Salisbury, M.H., Shinohara, M., Richter, C., et al., 2002
Proceedings of the Ocean Drilling Program, Initial Reports Volume 195

5. Site 1202[1]

Shipboard Scientific Party[2]

PRINCIPAL RESULTS

The Kuroshio (Black) Current is the biggest western boundary surface current in the western Pacific. Because of its high speed, great depth and width, and high temperature, it plays an important role in the meridional transport of heat, mass, momentum, and moisture from the western Pacific warm pool to high latitudes in the north Pacific. Although its role in the Pacific is as important as that of the Gulf Stream in the North Atlantic, almost nothing has been learned about its evolution during the past 32 yr of drilling by the Deep Sea Drilling Project (DSDP) and the Ocean Drilling Program (ODP) because there are almost no locations beneath the Kuroshio Current where a deep-sea sedimentary section with high sedimentation rates can contain well-preserved calcareous microfossils. The Southern Okinawa Trough is currently an area of high sedimentation because of the enormous terrigenous sediment supply from the East China shelf and the island of Taiwan. Modern sediments in this area consist mainly of clay- to silt-sized terrigenous sediments with a moderate (~20%) biogenic carbonate content. Site 1202 was proposed on the southern slope of the Okinawa Trough to obtain a high-resolution record of the history of the Kuroshio Current during the Quaternary.

Four holes were cored with the advanced hydraulic piston corer/extended core barrel (APC/XCB) at Site 1202, the deepest to a total depth of 410 meters below seafloor (mbsf). Logging efforts had to be abandoned because of strong drill pipe vibrations caused by strong currents at the site (occasionally >4.5 kt).

Because Site 1202 was drilled only a few hours out of port at the end of the leg, only minimal shipboard analysis, consisting of multisensor track (MST) and paleomagnetic studies on whole-round samples, preliminary dating of core catcher samples, sedimentological descriptions of split core from Hole 1202A, and whole-round sampling for shore-

[1]Examples of how to reference the whole or part of this volume.
[2]Shipboard Scientific Party addresses.

Ms 195IR-105

based geochemical studies was performed during Leg 195. Detailed descriptions of the core were prepared by a shore-based party assembled for the purpose at the ODP Gulf Coast Core Repository in College Station, Texas. The entire 410-m section recovered at Site 1202 consists of rapidly deposited dark gray calcareous silty clay and sandy turbidites. The oldest microfossils observed were <127 ka in age, making the sedimentation rate at least 325 cm/k.y.

BACKGROUND AND OBJECTIVES

Site 1202 was proposed to obtain a high-resolution record of the history of the Kuroshio Current during the Quaternary from the southern slope of the southernmost Okinawa Trough (Fig. F1). The Kuroshio (Black) Current is the biggest western boundary surface current in the western Pacific. It plays an important role in the meridional transport of heat, mass, momentum, and moisture from the western Pacific warm pool to high latitudes in the North Pacific. Although its role in the Pacific is as important as the Gulf Stream in the North Atlantic, virtually nothing has been learned about its evolution during the past 32 yr of drilling by DSDP and ODP. The lack of a deep-sea sedimentary record for the Kuroshio Current is due to the shallow carbonate compensation depth (<3500 m) and the great depth of the ocean (generally >4000 m) in the western Pacific. The only possible areas where adequate sequences could be obtained for such a study would be the marginal seas or shallow aseismic ridges located underneath the path of the Kuroshio Current. Site 1202, located in the southern end of the Okinawa Trough, represents one such ideal target. The selection of Site 1202 was based on excellent data sets collected recently during several international cooperative programs and integrated multidisciplinary studies. Of particular relevance are multiple lines of geophysical data accumulated over the past decade, including lines shot by the *Maurice Ewing* during 1995 (Fig. F2) and the swath-mapping survey of the French *L'Atlante* during the Active Collision in Taiwan (ACT) cruise in 1996. Recent imaging of volcanic seamounts and dredging of volcanic rocks and deep-sea biota by the southernmost part of the Okinawa Trough (SPOT) program (Lee et al., 1998a, 1998b) have added new insights into the tectonomagmatic evolution of the Okinawa Trough.

Oceanographic Setting and Late Quaternary Paleoceanography

The Kuroshio Current is characterized by its high speed (1.5–2 kt), narrow width (150–200 km), and great depth (~1000 m) (Fan, 1985; Yuan et al., 1998). It brings a great quantity (~22 sverdrup) (Yuan et al., 1998) of warm equatorial seawater northward while flowing along the east coast of the island of Taiwan (Nitani, 1972). It passes between the island of Tawian and the southernmost part of the Ryukyu Island arc and then flows northeastward along the Okinawa Trough (Ono et al., 1987) (Fig. F1). In the area immediately south of Site 1202, the Kuroshio Current appears to be deflected upward, causing upwelling when it approaches the Ilan Ridge (Chen et al., 1992b) (Fig. F1). The sea-surface temperatures of the Kuroshio Current off the eastern side of the island of Taiwan are ~28°–29°C in the summer and 22°–25°C in the winter. The salinity of the surface water is 33.6‰–34.8‰ (Hwang and Tang, 1993).

F1. Approximate path of the Kuroshio Current, p. 18.

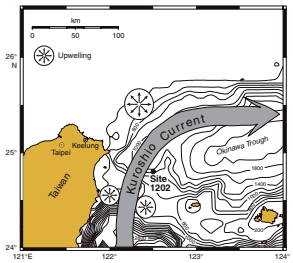

F2. North-south trending MCS reflection profile near Site 1202, p. 19.

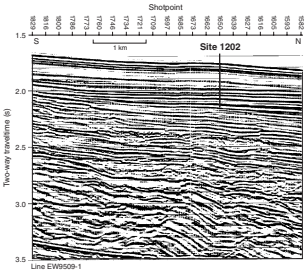

The Southern Okinawa Trough is an area of high sedimentation because of the enormous terrigenous sediment supply from the East China Sea shelf and from the island of Taiwan (Boggs et al., 1979; Lin and Chen, 1983; Chen et al., 1992b). Modern sediments in this area consist mainly of terrigenous material from rivers on nearby islands and secondarily of marine biogenic carbonates and opal, with a small portion of volcanic materials. The deposits in the vicinity of the drilling site are primarily clay- to silt-sized sediments with a moderate content of biogenic carbonate (~20%) (Chen et al., 1992b; Lou and Chen., 1996). Sediment trap studies in the southern Okinawa Trough (Hung et al., 1999) indicate that the abundance of suspended particulate matter decreases with increasing distance from the East Asian continent but increases with water depth, implying effective resuspension and lateral transport processes across this area. Studies of short piston cores (Lou and Chen, 1996; Shieh et al., 1997; Ujiié and Ujiié, 1999) taken from the area have provided estimates of Holocene sedimentation rates of ~20 cm/k.y.

Our current understanding of the past history of the Kuroshio Current is based on studies of short piston and gravity cores obtained from offshore areas off central Japan (e.g., Chinzei et al., 1987; Takemoto and Oda, 1997; Sawada and Handa, 1998) and the eastern side of the island of Taiwan (Chen et al., 1992a; Lou and Chen, 1996; Shieh et al., 1997). These studies emphasized glacial to interglacial (Chinzei et al., 1987; Oda and Takemoto, 1992; Takemoto and Oda, 1997) and millennial (Kallel et al., 1988; Sawada and Handa, 1998) variations.

It has been suggested that the Okinawa Trough changed from an open-sea environment to a semienclosed marginal basin because of a 120-m sea level drop (Fairbanks, 1989) during the last glacial maximum (Ujiié et al., 1991). Consequently, the Kuroshio Current might have moved east of the Ryukyu Island arc (Ujiié et al, 1991; Ahagon et al., 1993) and outside the Okinawa Trough until ~7.5 ka, during the Holocene (Shieh and Chen, 1995). Glacial–interglacial sea level fluctuations must have resulted in significant changes in the configuration and distribution of continental shelves in the region, particularly in the East China Sea. Consequently, such changes must have caused dramatic hydrographic changes and sediment redistribution in the Okinawa Trough.

Tectonic Background

The Okinawa Trough, extending from southwest Kyushu, Japan, to the northeast side of the island of Taiwan, is an active, incipient, intracontinental backarc basin formed behind the Ryukyu arc–trench system in the western Pacific (Lee et al., 1980; Letouzey and Kimura, 1985; Sibuet et al., 1987). The trough was formed by extension within continental lithosphere already intruded by arc volcanism (Uyeda, 1977; Sibuet and Hsu, 1997). There is considerable controversy about the age of the early rifting phase of the Okinawa Trough, although most researchers agree that the two most recent phases of extension have taken place since 2 Ma (Sibuet et al., 1998, and references therein). The southernmost part of the Okinawa Trough (southwest of 123°E) (Fig. **F1**) is characterized as a rifting basin with incipient arc volcanism opening in the middle of a foundered orogen caused by previous arc-continent collision (Teng, 1996). Wang et al. (1999) proposed that postcollisional lithospheric extension in the northern Taiwan mountain belt during the Pliocene–Pleistocene triggered the Pleistocene rifting in the middle Okinawa Trough, making room for its subsequent southwestward prop-

agation in association with the development of the southernmost Ryukyu subduction zone near the island of Taiwan.

The recent phase of extension of the Okinawa Trough occurred in late Pleistocene time (~0.1 Ma) (Furukawa et al., 1991), based on seismic correlation with drilling stratigraphy (Tsuburaya and Sata, 1985), but the exact timing of this recent phase of extension in the SPOT area is unknown. The extension is characterized by normal faults on both sides of the trough. The amount of extension during this recent phase has been estimated to be 5 km, both in the middle (Sibuet et al., 1995) and in the southwest end of the Okinawa Trough (Sibuet et al., 1998).

The penultimate rifting phase started at ~2 Ma (Sibuet et al., 1998). This assessment is based on the coincidence in timing between the development of the sedimentary basins of the Okinawa Trough (Kimura, 1985) and the uplift of the Ryukyu arc at the Pliocene/Pleistocene boundary (Ujiié, 1980). Sibuet et al. (1998) argued that the initiation of subsidence and block faulting along the central axis of the trough took place at ~2 Ma. The total amount of extension in the SPOT area is ~30 km.

Extensive marine geophysical surveys have been carried out in the southernmost Okinawa Trough, and detailed bathymetry data (Sibuet et al., 1998; Liu et al., 1998) and gravity and magnetic anomaly maps (Hsu et al., 1998) have been compiled. The major structural patterns in the Okinawa Trough are a series of normal faults dipping toward the center and a series of volcanic edifices piercing through the sedimentary layer. A prominent series of reflectors is observed from 250 to 350 ms below the seafloor (Fig. F2). This prominent reflection has been suggested to be the unconformity marking the onset of the most recent phase of extension of the southern Okinawa Trough (Hsu, 1999). Site 1202 was proposed to penetrate this sequence to a depth of ~410 mbsf. It was expected that the cores collected would not only address the paleoceanography of the Kuroshio Current, but would also provide constraints on the timing of the most recent phase of extension in the Okinawa Trough.

Objectives

Four major paleoceanographic objectives were identified for Site 1202. These include the following:

1. Identifying patterns of long-term climate change associated with the western Pacific boundary current during the past ~1.5 m.y.;
2. Examining the western Pacific component of long-term changes in orbital forcing in the mid-Pleistocene (~0.7 Ma) when the Earth's climate system switched from a regime of dominant 41- to 100-k.y. cycles;
3. Exploring any long-term El Niño/La Niña types of climate oscillations in the low-latitude Pacific during the late Pleistocene glacial–interglacial cycles by comparing the Kuroshio Current record to other ODP Pacific records (Andreasen and Ravelo, 1997; Clement et al., 1999); and
4. Documenting temporal and spatial variability of millennial climate changes in the vicinity of the Kuroshio Current.

OPERATIONS

Transit to Site 1202 (Proposed Site KS-1)

The transit to Site 1202 (proposed Site KS-1) was made in good time with fair seas and favorable currents. The 784-nmi distance was covered in 64.9 hr at an average speed of 12.1 kt. At 0254 hr on 28 April 2001, the vessel arrived at 24°48.24′N, 122°30.00′E, the coordinates for the drilling location. The crew began lowering thrusters and hydrophones, and at 0515 hr on 28 April, the positioning beacon was deployed.

Hole 1202A

A standard APC/XCB bottom-hole assembly, including a lockable float valve to allow wireline logging of the deepest hole of the site, was made up. The drill string was tripped to the bottom, and Hole 1202A was spudded at 0810 hr at 1274.1 mbsl. APC coring continued through Core 195-1202A-9H to a depth of 83.1 mbsf (Table T1), when the APC failed to stroke out. Core 195-1202A-10H fully stroked; however, Cores 11H and 12H did not fully advance. Advance by recovery was used for the two incomplete cores in the hope that the hard layer would be limited in thickness and piston coring would once again become viable. APC refusal was finally accepted when Core 195-1202A-13H at 119.5 mbsf had not only failed to scope, but the core liner failed at the midpoint of the barrel. Core orientation using the Tensor tool was initiated with Core 195-1202A-4H and continued through Core 13H. Temperature measurements were taken on Cores 195-1202A-4H, 7H, 10H, and 13H using the Adara temperature tool. Two of the four temperature measurements were good (see "Physical Properties," p. 11). The developmental APC-methane tool was deployed on Core 195-1202A-4H and then on Cores 7H through 13H. All runs were successful in acquiring data. Hole 1202A officially ended with the clearing of the seafloor at 1900 hr on 28 April.

T1. Coring summary, Site 1202, p. 41.

Hole 1202B

The vessel was offset 15 m to the east, and Hole 1202B was spudded at 1935 hr on 28 April at 1274.1 mbsl. APC coring continued through Core 195-1202B-13H to a depth of 111.6 mbsf (Table T1) before APC refusal was defined by two successive incomplete strokes on Cores 12H and 13H. Because the ultimate depth objective at this site was 410 mbsf, we decided to cut three XCB cores before terminating the hole to obtain an idea about penetration rates, core recovery, and quality. Coring continued with the XCB through Core 195-1202B-16X to a depth of 140.5 mbsf. The drill string was pulled clear of the seafloor, officially ending Hole 1202B at 0445 hr on 29 April.

Hole 1202C

The ship was offset 15 m to the east, and Hole 1202C was spudded at 0540 hr on 29 April at 1273.6 meters below sea level (mbsl). APC coring continued through Core 195-1202C-11H to a depth of 97.5 mbsf (Table T1), where APC refusal was encountered as defined by three consecutive incomplete strokes. Core orientation using the Tensor tool was initiated with Core 195-1202C-4H and continued through Core 11H. The

drill string was pulled clear of the seafloor, officially ending Hole 1202C at 1215 hr on 29 April.

Hole 1202D

For the third time, the ship was offset 15 m to the east, and Hole 1202D was spudded with the APC at 1245 hr on 29 April at 1275.1 mbsl. Recovery of the first core was only 15 cm. APC coring continued in this hole through Core 195-1202D-9H to a depth of 76.2 mbsf (Table T1), when the first core did not achieve full stroke. Coring with the XCB proceeded through Core 195-1202D-32X to a depth of 297.4 mbsf, where a short wiper trip was made to 221.3 mbsf, above an area of poor recovery. The wiper trip was uneventful, and coring continued through Core 195-1202D-44X to a depth of 410.0 mbsf, the approved target depth for Site 1202.

In preparation for logging, a wiper trip was initiated at 1930 hr on 30 April and reached the logging depth of 80.0 mbsf without incident. The hole was displaced with 150 bbl of sepiolite logging mud, and the bit was pulled back to a logging depth of 80.0 mbsf.

The triple combination tool string was made up with the Lamont-Doherty Earth Observatory (LDEO) temperature/acceleration/pressure (TAP) tool. A nuclear source was not incorporated because the loss of density data did not outweigh the risk of losing the source in disputed waters under hostile current conditions. Throughout operations at the site, the Kuroshio Current was very strong. Heavy pipe vibration was experienced continually while the currents varied cyclically between 2.6 and nearly 4.0 kt. The first tool string was deployed to a depth of ~215 meters below rig floor. At that point, the logging engineer reported losing all power to the logging tools. After bringing the tool string to the surface, the tools showed several loose connections, caused by the current-induced drill string vibrations. All joints were again tightened and taped with duct tape. The tool string was once again deployed inside the drill pipe; however, the winch operator only reached 72 mbsf before losing weight with the logging line as if setting down on an obstruction. Upon recovery, the connections were once again found to be loose and the lower portion of the TAP tool was missing.

At 0430 hr on 1 May, the circulating head was rigged up and the coring line was run in the hole to determine if the TAP tool was lodged in the drill string. Results were inconclusive. It was decided to abandon further wireline logging efforts because of the intensity of the current-induced drill string vibration. The drill string was pulled clear of the seafloor by 0730 hr. By 1100 hr, preparations were under way to secure and clean the ship for transit into port. The ~55-nmi transit to Keelung, Taiwan, was made in ~7 hr.

LITHOSTRATIGRAPHY

At Site 1202, four holes were drilled: 1202A, 1202B, 1202C, and 1202D. Time constraints limited shipboard sedimentological core processing to Hole 1202A, upon which visual core description and color photospectroscopy were performed. The remaining cores were processed and described at the ODP Gulf Coast Core Repository at Texas A&M University ~4 months postcruise, including smear slide analysis of sediment samples from Hole 1202D. Recovery was very good in three holes: 1202A (106.4%), 1202B (102%), and 1202C (105.2%) and good

in Hole 1202D (78.4%). The sedimentary succession consists of one lithostratigraphic unit, which is characterized by homogeneous, bioturbated clayey silt with isolated sandy intervals.

Unit I

Interval: Sections 195-1202A-1H-1, 0 cm, to 13H-CC, 95 cm; 195-1202B-1H-1, 0 cm, to 16X-CC, 36 cm; 195-1202C-1H-1, 0 cm, to 11H-CC, 34 cm; and 195-1202D-1H-1, 0 cm, to 44X-CC, 13 cm
Depth: 0–120.07; 0–139.33; 0–97.78; and 0–408.10 mbsf
Age: late Quaternary (<0.46 Ma)

Unit I extends through the entire recovered succession in Holes 1202A, 1202B, 1202C, and 1202D. The color of Unit I from Hole 1202A (described on board ship) was dark greenish gray. For the cores described at Texas A&M University, Unit I is dark gray and becomes predominantly olive downcore. The color difference between the shipboard and repository descriptions is likely attributable to oxidation of the cores during their transit to Texas A&M University and storage as whole cores for 4 months before splitting. Dark gray horizons (centimeter scale) first occur in Sections 195-1202A-8H-1, 195-1202B-5H-1, 195-1202C-4H-1, and 195-1202D-8H-1 and are common throughout the remainder of the core (Fig. F3). Dark gray mottling occurs throughout the cores but is concentrated in some intervals. Small (millimeter scale) black and brown mottles (burrows?) partly comprised of sand-sized material are common in the uppermost cores and streak vertically through the core during cutting. The entire section is slightly disrupted by horizontal gas voids.

Unit I is characterized by homogenous, slightly calcareous, bioturbated clayey silt with isolated sandy intervals and fine sand laminae. Macrofossils and shell fragments are rare but are visible in most sections. Some sandy intervals (<5 cm thick) are normally graded with sharp, erosive basal contacts (e.g., Sample 195-1202D-17X-5, 132–135 cm) (Fig. F4). There are rare occurrences of inversely graded fine sands (e.g., Sample 195-1202D-31X-6, 24–35 cm), laminae within sand intervals (e.g., Sample 195-1202D-16X-6, 9–11 cm), and medium to coarse sands that are not calcareous (e.g., Sample 195-1202D-32X-4, 66–69 cm). More commonly, however, sandy intervals react strongly with 10% HCl and have been identified as detrital carbonate in smear slides. Sandy laminae also occur as thin (<5 mm thick) discontinuous stringers, thin beds (<5 cm), or burrows (Fig. F5). Sandy intervals increase in abundance and thickness at Core 195-1202D-20X. At this point, the recovery in Hole 1202D, the only hole that penetrated to this depth, begins to decrease. This is likely due to the washing of unconsolidated sands downhole during drilling and suggests that thicker sandy units prevail throughout the interval of poor recovery. Downhole from Core 195-1202D-31X, the abundance and appearance of the sandy units resemble those described above the interval of poor recovery.

Smear Slide Analyses

Microscopic smear slide analyses were carried out on sediment samples from Hole 1202D and revealed low downcore variability in textural and compositional features (see "Site 1202 Smear Slides," p. 84). The major lithology consists of clayey silts, mostly with <25% clay and high abundances of medium to coarse silt. Intercalated sandy intervals com-

F3. Black centimeter-scale horizons, Unit I, p. 20.

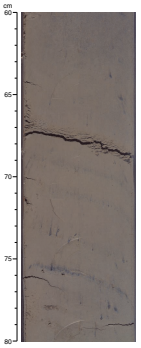

F4. Normally graded interval, Unit I, p. 21.

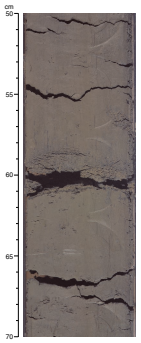

F5. Calcareous, sand-sized interval in silty clay, Unit I, p. 22.

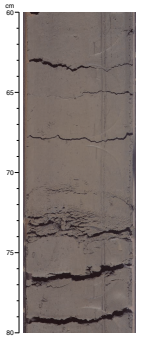

prise sandy silts and sands with proportions of fine-grained and medium sand between 25% and 70%.

In all lithologies, the nonbiogenic sediment fraction is dominated by quartz and feldspar grains and abundant detrital carbonate clasts. Clay minerals form part of the fine silt and clay fractions. Some of the larger sand grains represent lithoclasts derived from marls and calcareous mica schists. The sand and coarse silt fraction includes mica, heavy minerals, and opaque minerals in minor amounts (mostly <5%). Indentified heavy minerals are green hornblende, epidote, tourmaline, and zircon, but others might also be present. In Sample 195-1202D-17X-3, 113 cm, one grain of blue hornblende was recognized. Volcanic glass shards are rare and were only observed in Sample 195-1202D-14X-6, 120 cm.

Biogenic components are present in minor amounts (<20%). They consist of biosiliceous material, mostly diatom and radiolarian remains, and calcareous nannofossils. Foraminifers are rarely seen in smear slides. Biosiliceous remains tend to decrease downhole, with maximum amounts above 65 mbsf and rare amounts below 220 mbsf.

Environmental Interpretation

The sedimentological analysis at Site 1202 enables a few constraints to be identified regarding the depositional environment at this locality within the Okinawa Trough. The site is characterized by an extremely high sedimentation rate, possibly in excess of 3 m/k.y. (see **"Biostratigraphy,"** p. 8). This rate cannot be attributed to biological activity alone, as suggested by the low biogenic content, and implies a large terrigenous sediment input from an external source, likely reworked material from the shelf of the East China Sea supplied by turbidity currents through canyons to the Okinawa Trough. Clayey silts likely have been deposited by permanent contour currents, whereas graded sand layers indicate episodes of turbidity current activity. Thicker sandy intervals and relatively poor recovery beginning at Core 195-1202D-20X and continuing through 31X suggest that larger turbidity current events characterize this interval. Sources may include mountain ranges on the island of Taiwan, as suggested by detrital carbonate and high mica content, possibly from low-grade metamorphic schists and marls found within these ranges. The oceanic setting at Site 1202 north of the Ilan Sill, together with the high sedimentation rate, promotes nutrient upwelling and preservation of organic matter content as indicated by the dark color of the sediments and the smell of H_2S when opening the cores. No discrete ash layers were identified; however, preliminary smear slide analysis identified one sample with volcanic glass particles, indicating that the sediments likely include a small proportion of admixed ash particles. Discontinuous sand laminae, sand-filled burrows, and the homogeneous nature of the sediments suggest that bioturbation has reworked the core material extensively. Shallow-water foraminifers and wood fragments were identified within the coarse-grained component (see **"Biostratigraphy,"** p. 8).

BIOSTRATIGRAPHY

Core catchers from Holes 1202A, 1202B, and 1202D were examined for calcareous nannofossils. Well to moderately preserved nannofossils are present throughout the succession except for a sandy sample from

Section 195-1202D-28X-CC (253.24 mbsf) (Table T2). The age-diagnostic marker for nannofossil Zone NN21, *Emiliania huxleyi,* occurs persistently throughout the succession, suggesting that the recovered interval is younger than 0.26 Ma (latest Quaternary).

To detect the last extinction of pink *Globigerinoides ruber* at 127 ka (Thompson et al., 1979; Cang et al., 1988; Lee et al., 1999), core catchers and 19 additional samples from Hole 1202D were examined for foraminifers. Nevertheless, pink-pigmented *G. ruber* was not found. The persistent appearance of orange-colored tiny *Zeaglobigerina rubescens,* on the other hand, indicates that the sediments are young and fresh (Parker and Berger, 1971) despite their burial as deep as 410 mbsf.

Both nannofossils and planktonic foraminifers suggest that the cored succession is younger than 127 ka. The average sedimentation rate at Site 1202 is at least 320 cm/k.y.

Remains of copepods/crustaceans(?) and plants were occasionally found in samples, indicative of quick burial and high sedimentation rates.

Besides the commonly found planktonic and benthic foraminifers, sponge spicules and plates and spines of echinoderms are the major subordinate constituents. Fragments of pteropod shells and molluscs, valves of diatoms and ostracodes, and radiolarians are also found, especially in turbidite layers. In general, the washed residues of samples taken from muddy intervals yielded only a small quantity of planktonic and benthic foraminifers (<1% by volume) because of dilution by terrestrial clay and silts.

T2. Distribution of calcareous nannofossils, p. 44.

PALEOMAGNETISM

All core archive halves from Hole 1202A and whole-round sections from Holes 1202B and 1202D (Cores 195-1202B-1H through 10H and 195-1202D-1H through 10H) were measured on the shipboard pass-through superconducting rock magnetometer. Cores from Hole 1202C and the XCB section of Hole 1202D were not measured during Leg 195 because of time constraints. The XCB cores from Hole 1202D were left on board after Leg 195 and measured during Leg 196. Results are included in this report. Natural remanent magnetization (NRM) and remanent magnetization after one 20-mT alternating-field (AF) demagnetization step were measured at 5-cm intervals on Hole 1202A cores and Cores 195-1202B-1H through 5H. All other sections were AF demagnetized at 20 mT only. In situ orientation data were collected with the Tensor tool for APC cores from Holes 1202A and 1202C from below 30 mbsf. In addition, six oriented discrete samples (standard 8-cm^3 plastic cubes) were collected from the working halves of Hole 1202A samples for progressive AF demagnetization. Because of the suspected high concentrations of organic material, the magnetic signal is prone to be affected by the dissolution of fine-grained magnetite during core storage, as has been found on cores from the upwelling regions along the Californian and African margins (Richter et al., 1999; Yamazaki et al., 2000). For this reason, the discrete samples were also used for the short- and long-term monitoring of the stability of the magnetic intensity. All discrete samples were demagnetized at successive peak fields of 5, 10, 15, 20, 25, 30, 35, 40, 50, 60, 70, and 80 mT to verify the reliability of the split-core measurements. All samples yielded good principal component analyses (Kirschvink, 1980) with fits having an average maximum angular deviation of 2°. After the AF demagnetization, a 100-mT field

was imparted and the magnetic intensity and susceptibility was measured. This procedure was repeated daily, and samples were left on board for continued monitoring of the magnetic intensity and susceptibility at weekly intervals. The magnetic intensity of the uncooled samples decreased to 70% to 85% of the initial magnetization within 2 months (Fig. F6).

Natural Remanent Magnetization and Magnetic Susceptibility

Magnetic susceptibility measurements were made on whole cores from all four holes as part of the multisensor track measurements program (see "Physical Properties," p. 11). Magnetic susceptibility ranges from 1.23×10^{-4} to 1.12×10^{-3} (SI volume units) (Fig. F7) and shows very distinct features that allow hole-to-hole correlation (Fig. F8) and appear to be related to climate change.

A primary magnetic component is preserved in sediments from all four holes. All discrete samples were easily demagnetized by AF techniques and revealed an excellent demagnetization behavior (Fig. F9). The intensity of NRM after 20-mT demagnetization from all four holes is similar in magnitude and trend, ranging from to 8×10^{-4} to 2×10^{-2} A/m (Fig. F7).

Magnetostratigraphy

Magnetic inclinations and declinations from all four holes indicate that only the Brunhes (C1n) normal polarity chron (Berggren et al., 1995) is recorded in these sediments (Fig. F7). The geomagnetic field at the latitude of Site 1202 (24.8°) has an inclination of 42.2°, assuming a geocentric axial dipole model, which is sufficiently steep to determine magnetic polarity in APC and XCB cores that lack a horizontal orientation. Whether the Brunhes Chron is complete cannot be determined from the magnetostratigraphy. However, preliminary biostratigraphic datums (see "Biostratigraphy," p. 8) indicate an age of <127 ka in Hole 1202D.

The intensity of NRM is controlled by the strength of the geomagnetic field, the concentration of magnetic minerals, and other rock-magnetic characteristics of sediments, including grain size, composition, and interaction of magnetic minerals. If the sediments prove to be magnetically uniform, variations of remanent intensity identified after normalization for the abundance of magnetic minerals using rock-magnetic parameters could be interpreted as relative changes of past geomagnetic field strength (paleointensity). Because relative paleointensity variations during the last 800 k.y. are relatively well understood (Guyodo and Valet, 1996, 1999), paleointensity can be used as a tool to correlate and date the age of sediments (paleointensity stratigraphy). Preliminary rock magnetic data indicate that the recovered material from Site 1202 is magnetically homogenous enough for a relative paleointensity determination, which can potentially be used to obtain a high-resolution age model within the Brunhes Chron (Guyodo and Valet, 1996, 1999).

The magnetic inclinations show a potentially excellent paleosecular variation record in the APC section but become noisy in the XCB cores (Fig. F7) because of the core disturbance and a steep vertical magnetic overprint imparted by the coring process. An interval of negative polar-

F6. Magnetic intensity behavior over time, p. 23.

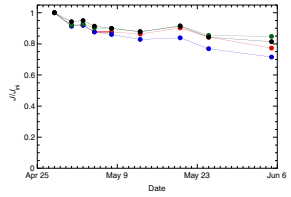

F7. Downcore magnetic inclination and intensity, p. 24.

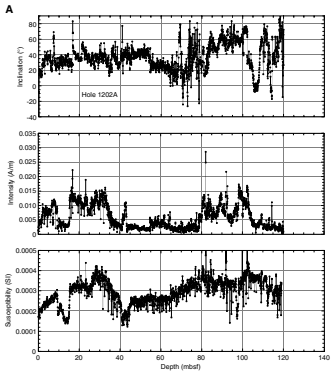

F8. Magnetic susceptibility, p. 27.

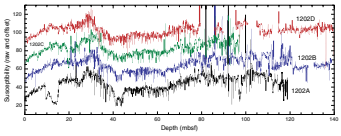

F9. Vector component diagram with intensity decay plots, p. 28.

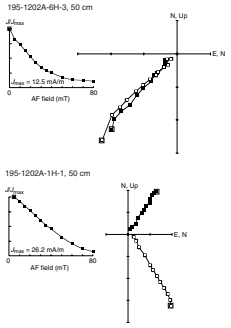

ity in Hole 1202A occurs between 105 and 108 mbsf. The same interval in Hole 1202B reaches shallow positive inclinations between 101 and 104 mbsf. It is possible that this interval represents one of the short geomagnetic excursions within the Brunhes Chron. Several excursions are well documented, such as the Mono Lake and Laschamp reversal excursions. The Mono Lake Excursion is only found in western North America and in the Arctic Seas and has an age of ~25 ka (Nowaczyk et al., 1994). The Laschamp Excursion is well established and radiometrically dated in France and Iceland (Levi et al., 1990), Hawaii (Holt et al., 1996), and the Arctic Sea (Nowaczyk et al., 1994). The age of the Laschamp Event ranges from 40 to 45 ka. It is possible that the polarity change at 110 mbsf represents the more globally occurring Laschamp Event, but more detailed studies are needed to confirm this interpretation.

PHYSICAL PROPERTIES

Whole-round core samples from Holes 1202A, 1202B, 1202C, and 1202D were run through the MST during Leg 195 if they were >40 cm long. These samples were collected from depths between 0 and 140 mbsf. Additional core recovered from depths between 140 and 410 mbsf in Hole 1202D were run through the MST during Leg 196 because time constraints did not permit measurement of this material during Leg 195.

The MST measured the volume magnetic susceptibility (MSL), the density using gamma ray attenuation (GRA), and the *P*-wave velocity. The *P*-wave velocity logger (PWL) was able to obtain *P*-wave velocity measurements only to a depth of 20 mbsf.

Vane shear strength measurements were made on samples from Hole 1202A, the only cores from Site 1202 split during Leg 195. Thermal conductivity measurements were made on every core run through the MST. Because of time constraints, no index properties samples were taken at Site 1202.

Volume Magnetic Susceptibility

Variation of the volume magnetic susceptibility is often used as a proxy for climate change. It was measured at Site 1202 on cores from all four holes to obtain a continuous record of the magnetic susceptibility signal; the records from the individual holes overlap and can potentially be spliced into a single record with no coring gaps. Figure **F10** shows the magnetic susceptibility of samples recovered from Holes 1202A, 1202B, 1202C, and 1202D to a depth of 140 mbsf. At a scale of several meters, the records show an excellent correlation between holes. At smaller scales (<1 m) the amount of noise in the records may preclude correlation between holes. This noise is caused by gas expansion voids and by coring deformation in the XCB parts of the section. Figure **F11** compares the volume magnetic susceptibility of samples recovered from 0 to 420 mbsf in Hole 1202D measured during Leg 196 with the volume magnetic susceptibility values from 0 to 140 mbsf measured during Leg 195. This graph shows that there is excellent agreement between the measurements made during Leg 195 and those made during Leg 196. The magnetic susceptibility did not change over time, so the measurements made on the lower samples (140–420 mbsf) are reliable.

F10. Volume magnetic susceptibility, p. 29.

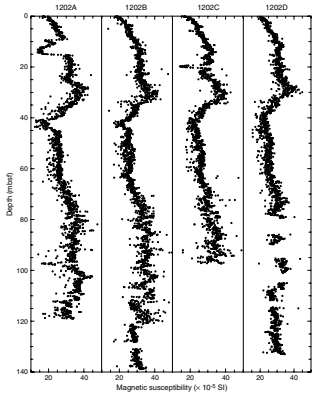

F11. MST volume magnetic susceptibility, Hole 1202D, p. 30.

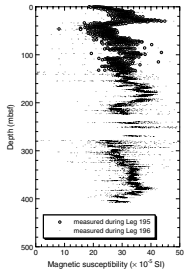

In addition, the variability and range of the lower measurements (140–420 mbsf) are similar to the upper measurements (0–140 mbsf).

The largest value of magnetic susceptibility is equal to 6000×10^{-5} (SI units) at a depth of ~85 mbsf in Hole 1202D (this peak is off the scale of Fig. F11). The depths of the largest values of magnetic susceptibility are similar in the other three holes. These values may indicate a thin layer of high-susceptibility material. Another peak of lesser magnitude (nearly 400×10^{-5} SI units) is present at a depth of 293 mbsf in Hole 1202D. This peak is also off the scale of Figure F11.

Density

The results of the GRA bulk density measurements for Holes 1202A, 1202B, 1202C, and 1202D from a depth of 0–140 mbsf are shown in Figure F12. The densities measured in the four holes are all lowest near the seafloor, between 1.6 and 1.8 g/cm³, and increase to ~2.0 g/cm³ at 10–15 mbsf.

As was observed for the MSL measurements, the density records correlate at a scale of several meters. Again, the noise introduced by gas fractures and XCB drilling disturbance could make correlation difficult at a smaller scale. As a result, the largest density values will provide the best estimates of the bulk density for these sediments. The decrease in density between 80 and 90 mbsf corresponds to an increase in magnetic susceptibility shown in Figure F10.

A comparison of the GRA bulk density measurements made during Legs 195 and 196 on samples from Hole 1202D is shown in Figure F13. This graph shows that the measurements made during Leg 196 are reduced by ~0.3–0.5 g/cm³ from the Leg 195 measurements for the same depths (0–140 mbsf). The cause of this reduction in GRA densities is almost certainly dessication or pooling of water at the liner bottom, since the core liners were systematically perforated immediately after recovery to allow gas to escape. The values of GRA density measured during Leg 196 are thus suspect and should not be used to estimate the density of the sediments.

Porosity (ϕ) was calculated from the GRA bulk density using Equation 1, which assumes generic values of 2.7 g/cm³ for the grain density and 1.0 g/cm³ for the pore water density. The porosities calculated are plotted vs. depth for all four holes in Figure F14. Although the data show significant scatter inherited from the variability in the density data, porosity clearly decreases overall with increasing depth, from between 50% and 70% at the seafloor to between 40% and 60% at a depth of ~120 mbsf:

$$\phi = (\rho_{grain} - \rho_{bulk})/(\rho_{grain} - \rho_{pore\ water}). \quad (1)$$

NGR

The results of natural gamma radiation (NGR) emissions measured during Leg 196 on core recovered from Hole 1202D are shown in Figure F15. The rate of NGR emissions is relatively high throughout the section. The variations follow the GRA density measurements more closely than the magnetic susceptibility measurements, particularly in the first 50 mbsf. There is an overall increasing trend from 30 counts per second (cps) at the seafloor to a maximum of 60 cps at 380 mbsf. The count rate increases most in the first 10 m below the seafloor to a peak of ~47

F12. Bulk density results, p. 31.

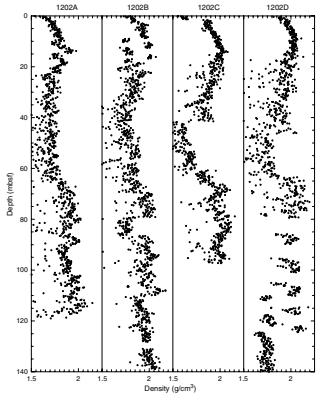

F13. GRA bulk density results, p. 32.

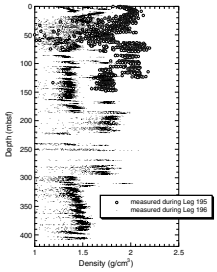

F14. Porosity derived from GRA density, p. 33.

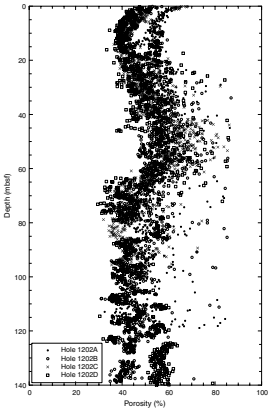

F15. Natural gamma radiation, Hole 1202D, p. 34.

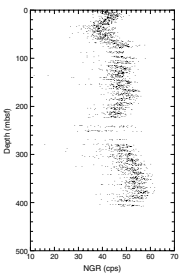

cps. Between 30 and 70 mbsf, there is a distinct drop in emissions to ~40 cps.

P-Wave Velocity

The PWL measured sediment velocities in the four holes to a maximum depth of 20 mbsf. Below 20 mbsf, the PWL was unable to measure velocities because the cores developed voids and small cracks from gas expansion and poor coupling between the core and core liner caused attenuation of the signal. The velocities shown in Figure **F16** are typical of ocean-bottom sediments at shallow burial depths. They show a slight increase of velocity with depth from ~1.5 km/s at the seafloor to nearly 1.6 km/s at a depth of 20 mbsf. The large amount of scatter in the data is likely caused by the gas expansion voids and poor liner coupling.

Shear Strength

The shear strength of the sediments from Hole 1202A was measured once per core in the working half of the core within 30 min of splitting. The peak shear strengths are shown in Table **T3** and Figure **F17.** The peak shear strength increases nearly linearly with increasing depth from ~0 kPa at the seafloor to 45 kPa at 110 mbsf. The highest shear strength measured in Hole 1202A, 53 kPa at 77 mbsf, is almost double that predicted by the trend of all the other measurements and does not correspond to any obvious increases in density at the same depth (Fig. **F12**).

Thermal Conductivity

Thermal conductivity measurements (Fig. **F18**) show relatively little variation with depth and low scatter around a mean value of 1.04 W/(m·K). Occasional low values in the upper 50 m are probably caused by the presence of voids in the core formed by gas expansion. Thermal conductivity increases from ~1 W/(m·K) at the seafloor to a maximum of ~1.3 W/(m·K) at ~10 mbsf and then falls back to ~1 W/(m·K) by 30 mbsf and remains roughly constant to 250 mbsf. At depths >250 mbsf, the values become more variable but there are insufficient measurements to identify any trend.

Temperature Measurements

In situ temperature measurements were made in Hole 1202A using the Adara temperature probe. These temperature records are shown in Figure **F19.** Also shown on the figure are the seafloor or mudline temperature (T_{ml}) and the estimated sediment temperature at depth (T_{sed}).

The sediment temperatures at depth were determined using the curve fitting program TFIT. The estimates of sediment temperature can vary several degrees, depending on the value of the thermal conductivity of the sediment and the region of the decay curve chosen for the estimation. The estimated sediment temperatures shown in Figure **F19** were determined using only the latter portion of the middle temperature series, the temperature decay curves.

The mudline temperature was determined to be 4.6°C for the two measurements. The sediment temperature at a depth of 64.1 mbsf was 7.2°C, giving a thermal gradient of 0.04°C/m. The sediment temperature at a depth of 119.5 mbsf was 9.3°C, giving the same thermal gradient. The integrated thermal resistivity, calculated as the area under the

F16. *P*-wave velocity, p. 35.

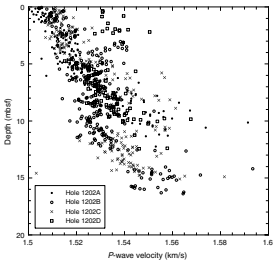

T3. Physical properties, p. 46.

F17. Peak shear strength, p. 36.

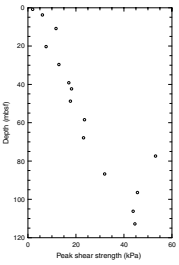

F18. Thermal conductivity, p. 37.

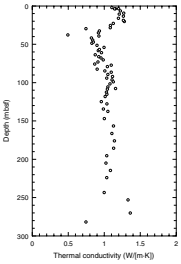

F19. Temperature measurements, p. 38.

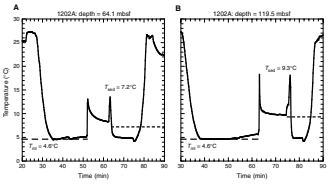

curve of depth vs. the inverse of the measured thermal conductivity, is shown in Figure **F20.** Temperatures (from Fig. **F19**) and integrated thermal resistivities corresponding to equivalent depths (from Fig. **F20**) are plotted in Figure **F21.** The slope of the best-fit line through the three points gives a heat flow for the site of 0.040 W/m², slightly less than the approximate global average of 0.050 W/m² (Garland, 1979). The linearity of the three points in Figure **F21** indicates a constant heat flow at this site.

F20. Integrated thermal resistivity vs. depth, p. 39.

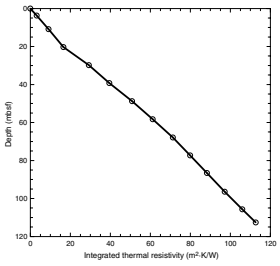

F21. Temperature vs. integrated thermal resistivity, p. 40.

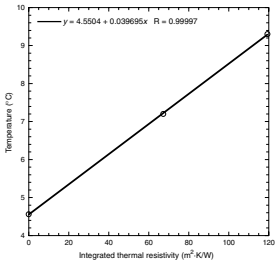

REFERENCES

Ahagon, N., Tanaka, Y., and Ujiié, H., 1993. *Florisphaera profunda,* a possible nannoplankton indicator of late Quaternary changes in sea-water turbidity at the northwestern margin of the Pacific. *Mar. Micropaleontol.,* 22:255–273.

Andreasen, D.J., and Ravelo, A.C., 1997. Tropical Pacific Ocean thermocline depth reconstructions for the last glacial maximum. *Paleoceanography,* 12:395–413.

Berggren, W.A., Kent, D.V., Swisher, C.C., III, and Aubry, M.-P., 1995. A revised Cenozoic geochronology and chronostratigraphy. *In* Berggren, W.A., Kent, D.V., Aubry, M.-P., and Hardenbol, J. (Eds.), *Geochronology, Time Scales and Global Stratigraphic Correlation*. Spec. Publ.—Soc. Econ. Paleontol. Mineral., 54:129–212.

Boggs, S., Jr., Wang, W.C., Lewis, F.S., and Chen, J.-C., 1979. Sediment properties and water characteristics of the Taiwan shelf and slope. *Acta Oceanogr. Taiwanica,* 10:10–49.

Cang, S., Shackleton, N.J., Qin, Y., and Yan, J. 1988. The discovery and significance of *Globigerinoides ruber* (pink-pigmented) in Okinawa Trough. *Mar. Geol. Quat. Geol.,* 8:24–29.

Chen, M.-P., Huang, C.-K., Lo, L., and Wang, C.-H., 1992a. Late Pleistocene paleoceanography of the Kuroshio Current in the area offshore Southeast Taiwan. *TAO,* 3:81–110.

Chen, M.-P., Lo, S.-C., and Lin, K.-L., 1992b. Composition and texture of surface sediment indicating the depositional environments off Northeast Taiwan. *TAO,* 3:395–417.

Chinzei, K., Fujioka, K., Kitazato, H., Koizumi, I., Oba, T., Oda, M., Okada, H., Sakai, T., and Tanimura, Y., 1987. Postglacial environmental change of the Pacific Ocean off the coast of central Japan. *Mar. Micropaleontol.,* 11:273–291.

Clement, A.C., Seager, R., and Cane, M.A., 1999. Orbital controls on the El Nino/Southern Oscillation and the tropical climate. *Paleoceanography,* 14:441–456.

Fairbanks, R.G., 1989. A 17,000-year glacio-eustatic sea level record: influence of glacial melting rates on the Younger Dryas event and deep-ocean circulation. *Nature,* 342:637–642.

Fan, K.L., 1985. *CTD Measurements in the Seas Around Taiwan During 1977–1983*. Spec. Publ.—Inst. Oceanogr., Natl. Univ. (Taiwan), 51.

Furukawa, M., Tokuyama, H., Abe, S., Nishizawa, A., and Kinoshita, H., 1991. Report on DELP 1988 cruises in the Okinawa trough. *Bull. Earthquake Res. Inst., Univ. Tokyo,* 66:17–36.

Garland, G.D., 1979. *Introduction to Geophysics:* Philadelphia (Saunders).

Guyodo, Y., and Valet, J.-P., 1996. Relative variations in geomagnetic intensity from sedimentary records: the past 200,000 years. *Earth. Planet. Sci. Lett.,* 143:23–36.

————, 1999. Global changes in intensity of the Earth's magnetic field during the past 800 kyr. *Nature,* 399:249–252.

Holt, J.W., Kirschvink, J.L., and Garnier, F., 1996. Geomagnetic field inclinations for the past 400 kyr from the 1-km core of the Hawaii Scientific Drilling Project. *J. Geophys. Res.*, 101:11655–11663.

Hsu, B.-H., 1999. Geological structure of South Okinawa Trough: A reflection seismic interpretation [MS Thesis]. National Central Univ., Taiwan. (In Chinese).

Hsu, S.-K., Liu, C.-S., Shyu, C.-T., Liu, S.-Y., Sibuet, J.-C., Lallemand, S., Wang, C.S., and Reed, D., 1998. New gravity and magnetic anomaly maps in the Taiwan Luzon region and their preliminary interpretation. *TAO,* 9:509–532.

Hung, J.-J., Lin, C.S., Hung, G.-W., and Chung, Y.-C., 1999. Lateral transport of lithogenic particles from the continental margin of the southern East China Sea. *Estuarine Coastal Shelf Sci.,* 49:483–499.

Hwang, S.J., and Tang, T.Y., 1993. CTD data bank data report. Regional Instrument Center *R/V Ocean Researcher I:* Taipei (Nat. Sci. Counc.).

Kallel, N., Labeyrie, L.D., Arnold, M., Okada, H., Dudley, W.C., and Duplessy, J.-C., 1988. Evidence of cooling during the Younger Dryas in the western North Pacific. *Oceanol. Acta,* 11:369–375.

Kimura, M., 1985. Back-arc rifting in the Okinawa Trough. *Mar. Pet. Geol.,* 2:222–240.

Kirschvink, J.L., 1980. The least-squares line and plane and the analysis of palaeomagnetic data. *Geophys. J. R. Astron. Soc.,* 62:699–718.

Lee, C.-S., Chiang, F., Kong, S.L., Chung, S.-L., and Lo, C.-H., 1998a. Kinematics of the opening of the southernmost part of Okinawa Trough. *Eos, Trans., Am. Geophys. Union,* 79:120. (Abstract).

Lee, C.-S., Shor, G.-G., Bibee, L.D., Jr., Lu, R.-S., and Hilde, Y.W.C., 1980. Okinawa Trough: origin of a back-arc basin. *Mar. Geol.,* 35:219–241.

Lee, C.-S., Tsai, C.-F., Chung, S.-L., and the SPOT members, 1998b. Active interaction of submarine volcanoes and ocean current in the southernmost part of Okinawa Trough. *Eos, Trans., Am. Geophys. Union,* 79:858. (Abstract).

Lee, M.-Y., Wei, K.-Y., and Chen, Y.-G., 1999. High resolution oxygen isotope stratigraphy for the last 150,000 years in the southern South China Sea: Core MD972151. *Terr., Atmos. Oceanic Sci.,* 10:239–254.

Letouzey, J., and Kimura, M., 1985. Okinawa trough genesis: structure and evolution of a back arc basin developed in a continent. *Mar. Pet. Geol.,* 2:111–130.

Levi, S., Audunsson, H., Duncan, R.A., Kristjansson, L., Gillot, P.Y., and Jakobsson, S., 1990. Late Pleistocene geomagnetic excursion in Icelandic lavas: confirmation of the Laschamps excursion. *Earth Planet. Sci. Lett.,* 96:443–457.

Lin, F.-T., and Chen, J.-C., 1983. Textural and mineralogical studies of sediments from the southern Okinawa Trough. *Acta Oceanogr. Taiwanica,* 14:26–41.

Liu, C.-S., Liu, S.Y., Lallemand, S.E., Lundberg, N., and Reed, D., 1998. Digital elevation model offshore Taiwan and its tectonic implications. *TAO,* 9:705–738.

Lou, J.-Y., and Chen, A.C.-T., 1996. A paleoenvironmental record during 7–21 Ka BP in the sediments off northern Taiwan. *Le Mer,* 34:237–245.

Nitani, H., 1972. Beginning of the Kuroshio. *In* Stommel, H., and Yoshida, K. (Eds.), *Kuroshio:* Seattle (Univ. Washington Press), 129–163.

Nowaczyk, N.R., Frederichs, T.W., Eisenhauer, A., and Gard, G., 1994. Magnetostratigraphic data from late Quaternary sediments from the Yermak Plateau, Arctic Ocean: evidence for four geomagnetic polarity events within the last 170 Ka of the Brunhes Chron. *Geophys. J. Int.,* 117:453–471.

Oda, M., and Takemoto, A., 1992. Planktonic foraminifera and paleoceanography in the domain of the Kuroshio Current around Japan during the last 20,000 years. *Quat. Res.,* 31:341–357.

Ono, T., Yamamoto, S., and Ujiié, H., 1987. Fluctuation of carbonate and interstitial-exchangeable elements in sediments from the ocean surrounding the Ryukyu Islands. *Compass,* 64:195–206.

Parker, F.L., and Berger, W.H., 1971. Faunal and solution patterns of planktonic foraminifera in surface sediments of the South Pacific. *Deep-Sea Res. Part A,* 18:73–107.

Richter, C., Hayashida, A., Guyodo, Y., Valet, J.-P., and Verosub, K.L., 1999. Magnetic intensity loss and core diagenesis in long-core samples from the East Cortez Basin and the San Nicolas Basin (California Borderland). *Earth, Planets Space,* 51:329–336.

Sawada, K., and Handa, N., 1998. Variability of the path of the Kuroshio ocean current over the past 25,000 years. *Nature,* 392:592–595.

Shieh, Y.-T., and Chen, M.-P., 1995. The ancient Kuroshio Current in the Okinawa Trough during the Holocene. *Acta Oceanogr. Taiwanica,* 34:73–80.

Shieh, Y.-T., Wang, C.-H., Chen, M.-P., and Yung, Y.-L., 1997. The last glacial maximum to Holocene environment changes in the southern Okinawa Trough. *J. Asian Earth Sci.,* 15:3–8.

Sibuet, J.-C., Deffontaines, B., Hsu, S.-K., Thareau, N., Formal, J.-P., Liu, C.-S., and the ACT Party, 1998. Okinawa Trough backarc basin: early tectonic and magmatic evolution. *J. Geophys. Res.,* 103:30245–30267.

Sibuet, J.-C., and Hsu, S.-K., 1997. Geodynamics of the Taiwan arc-arc collision. *Tectonophysics,* 274:221–251.

Sibuet, J.-C., Hsu, S.-K., Shyu, C.-T., and Liu, C.-S., 1995. Structural and kinematic evolution of the Okinawa Trough backarc basin. *In* Taylor, B. (Ed.), *Backarc Basins: Tectonics and Magmatism:* New York (Plenum Press), 343–378.

Sibuet, J.-C., Letouzey, J., Barbier, F., Charvet, J., Foucher, J.-P., Hilde, T.W.C., Kimura, M., Ling-Yun, C., Marsett, B., Muller, C., and Stephan, J.-F., 1987. Back arc extension in the Okinawa Trough. *J. Geophys. Res.,* 92:14041–14063.

Takemoto, A., and Oda, M., 1997. New planktic foraminiferal transfer functions for the Kuroshio-Oyashio Current region off Japan. *Paleontol. Res.,* 1:291–310.

Teng, L.S., 1996. Extensional collapse of the northern Taiwan mountain belt. *Geology,* 24:949–952.

Thompson, P.R., Bé, A.W.H., Duplessy, J.-C., and Shackleton, N.J., 1979. Disappearance of pink-pigmented *Globigerinoides ruber* at 120,000 yr BP in the Indian and Pacific Oceans. *Nature,* 280:554–558.

Tsuburaya, H., and Sata, T., 1985. Petroleum exploration well Miyakojima-Oki. *J. Japanese Assoc. Petrol. Technol.,* 50:25–53.

Ujiié, H., 1980. Significance of "500 m deep island shelf" surrounding the southern Ryukyu island arc for its Quaternary history. *Quat. Res.,* 18:209–219.

Ujiié, H., Tanaka, Y., and Ono, T., 1991. Late Quaternary paleoceanographic record from the middle Ryukyu Trench slope, northwest Pacific. *Mar. Micropaleontol.,* 18:115–128.

Ujiié, H., and Ujiié, Y., 1999. Late Quaternary course changes of the Kuroshio Current in the Ryukyu arc region, northwestern Pacific Ocean. *Mar. Micropaleontol.,* 37:23–40.

Uyeda, S., 1977. Some basic problems in the trench-arc-back-arc system. *In* Talwani, M., and Pittman, W.C., II (Eds.), *Island Arcs, Deep Sea Trenches, and Back-arc Basins.* Am. Geophys. Monogr., Maurice Ewing Ser., Am. Geophys. Union, 1–14.

Wang, K.L., Chung, S.-L., Chen, C.-H., Shinjo, R., Yang, T.-F., and Chen, C.-H., 1999. Post-collisional magmatism around northern Taiwan and its relation with opening of the Okinawa Trough. *Tectonophysics,* 308:363–376.

Yamazaki, T., Solheid, P.A., and Frost, G.M., 2000. Rock magnetism of sediments in the Angola-Namibia upwelling system with special reference to loss of magnetization after core recovery. *Earth, Planets Space,* 52:329–336.

Yuan, Y., Liu, Y., Liu, C.-T., and Su, J., 1998. The Kuroshio east of Taiwan and the currents east of the Ryukyu Islands during October of 1995. *Acta Oceanol. Sin.,* 17:1–13.

Figure F1. Approximate path of the Kuroshio Current in the area of Site 1202. Diverging arrows indicate areas of upwelling (modified after Chen et al., 1992b).

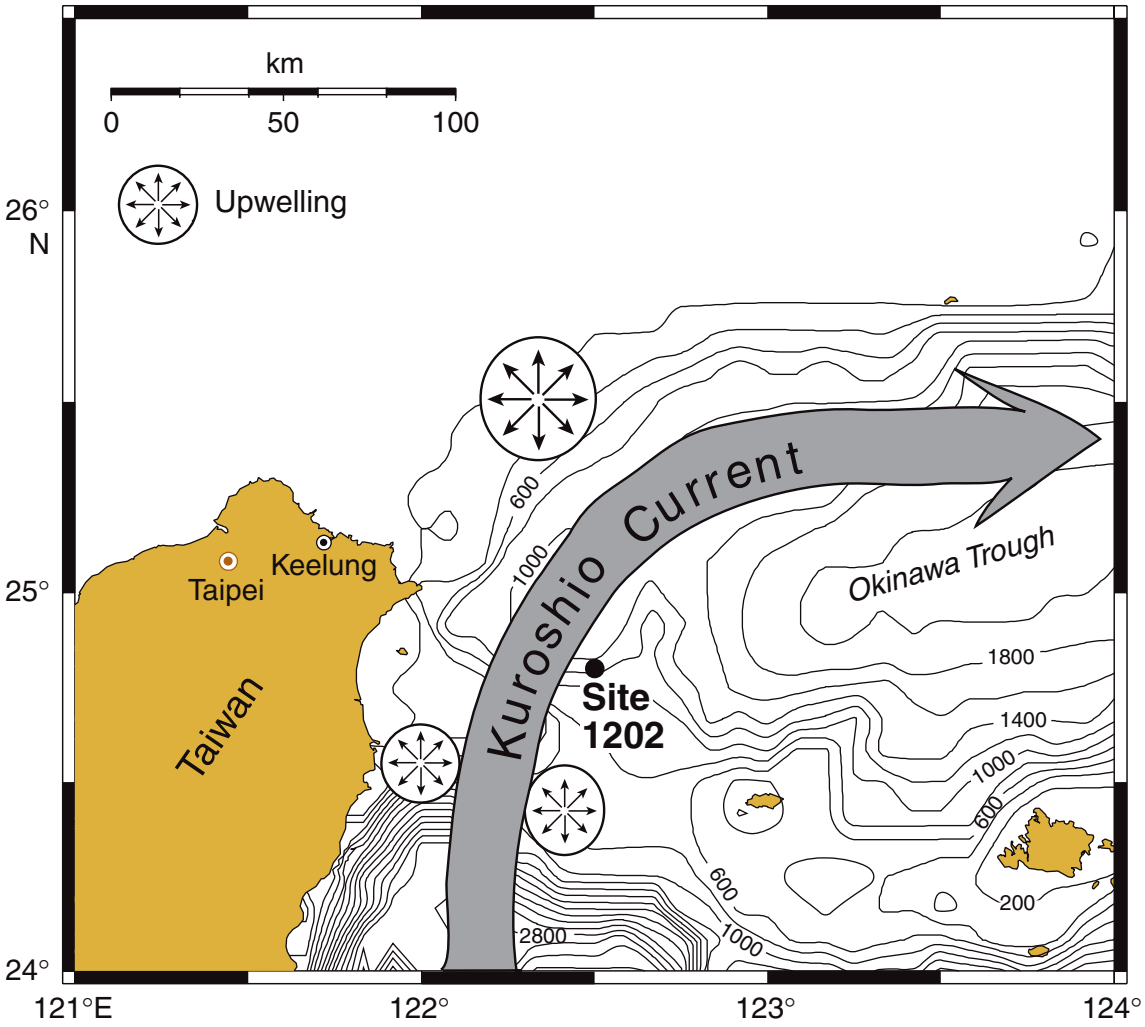

Figure F2. North-south trending multichannel seismic reflection profile EW9509-1 in the vicinity of Site 1202.

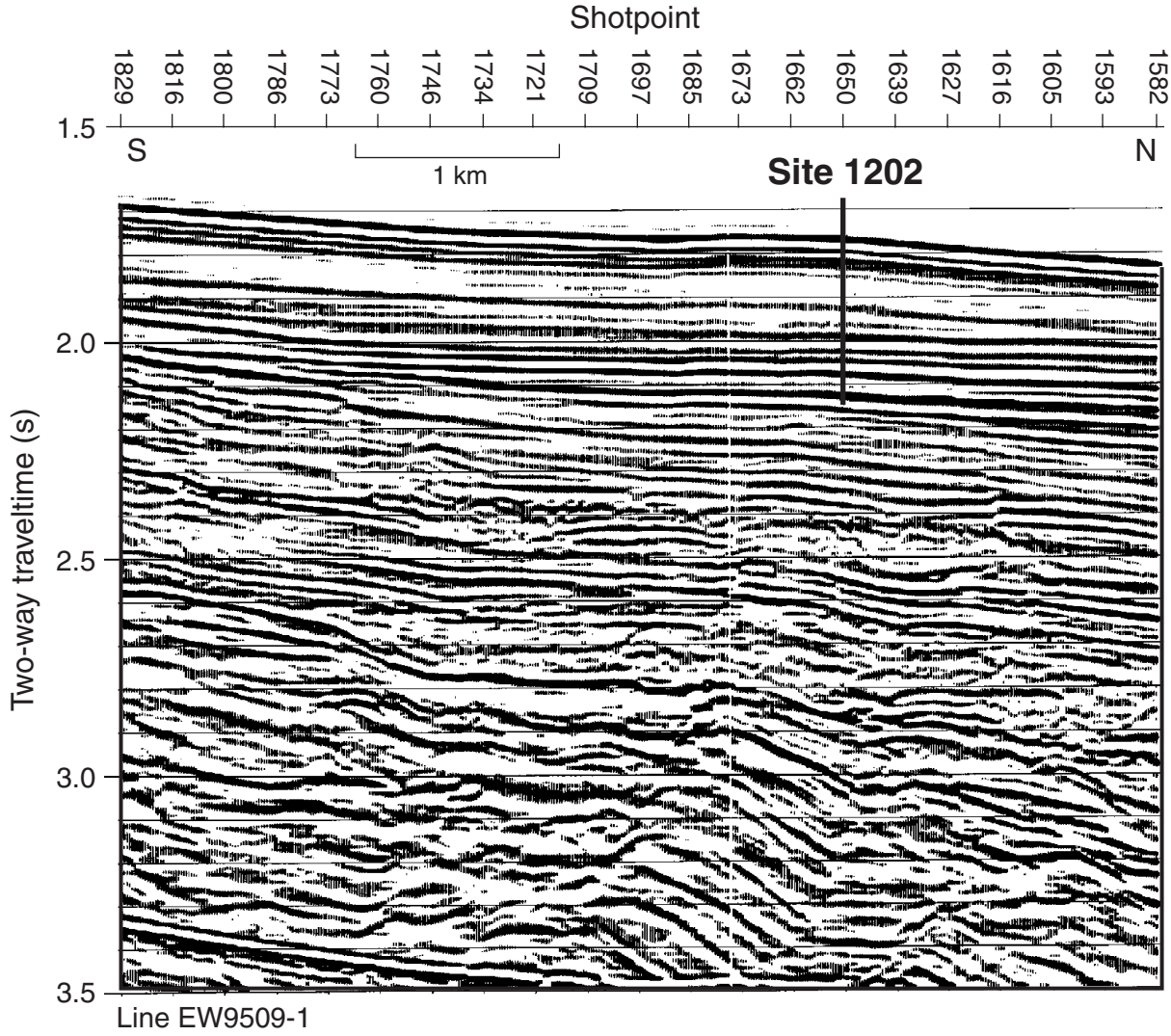

Figure F3. Black centimeter-scale horizons in Unit I. Note the calcareous, sand-sized interval from 66 to 68 cm (interval 195-1202A-9H-5, 60–80 cm).

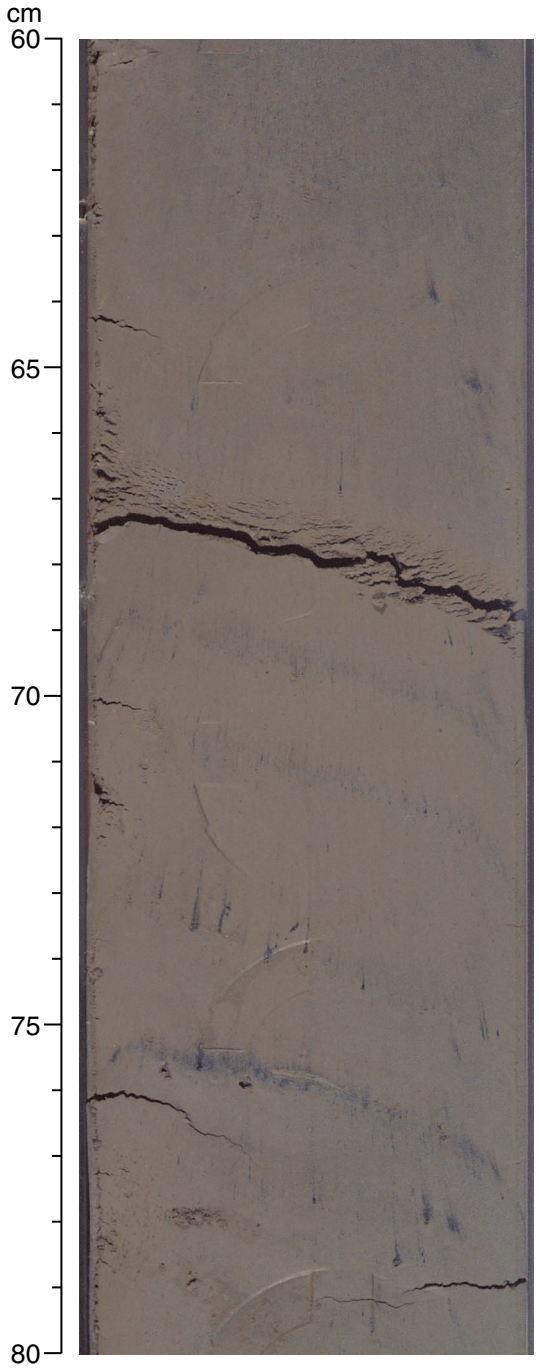

Figure F4. Normally graded interval in Unit I. The basal contact is sharp and erosive. The coarsest component is composed of calcareous, sand-sized fragments (interval 195-1202A-3H-5, 50–70 cm).

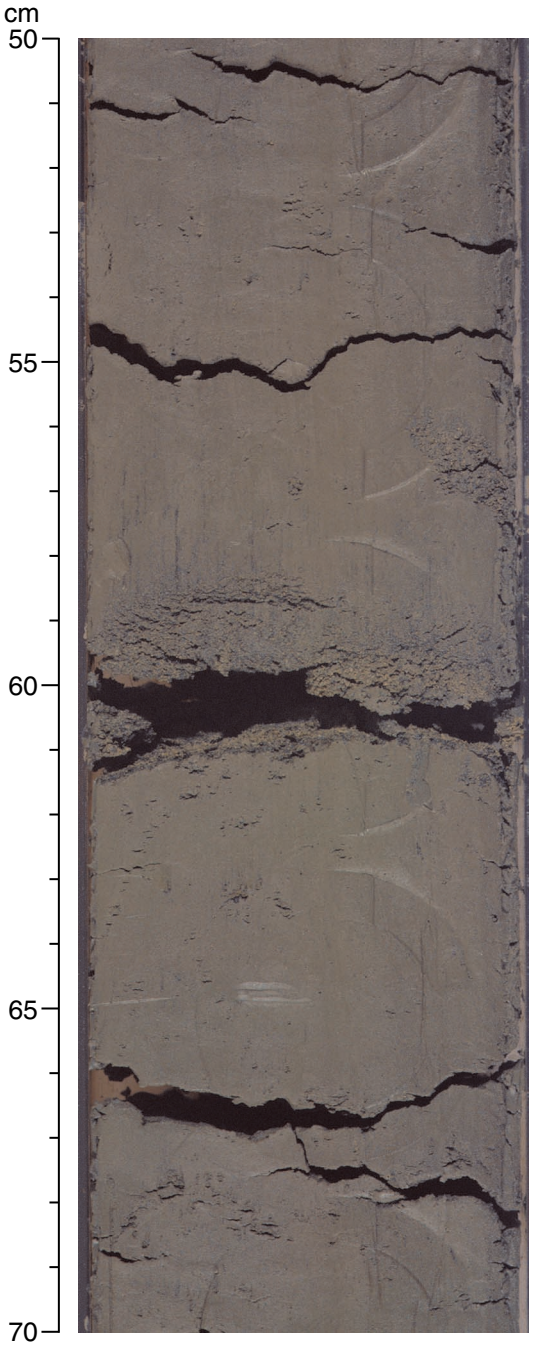

Figure F5. Calcareous, sand-sized interval in silty clay of Unit I (interval 195-1202A-4H-4, 60–80 cm).

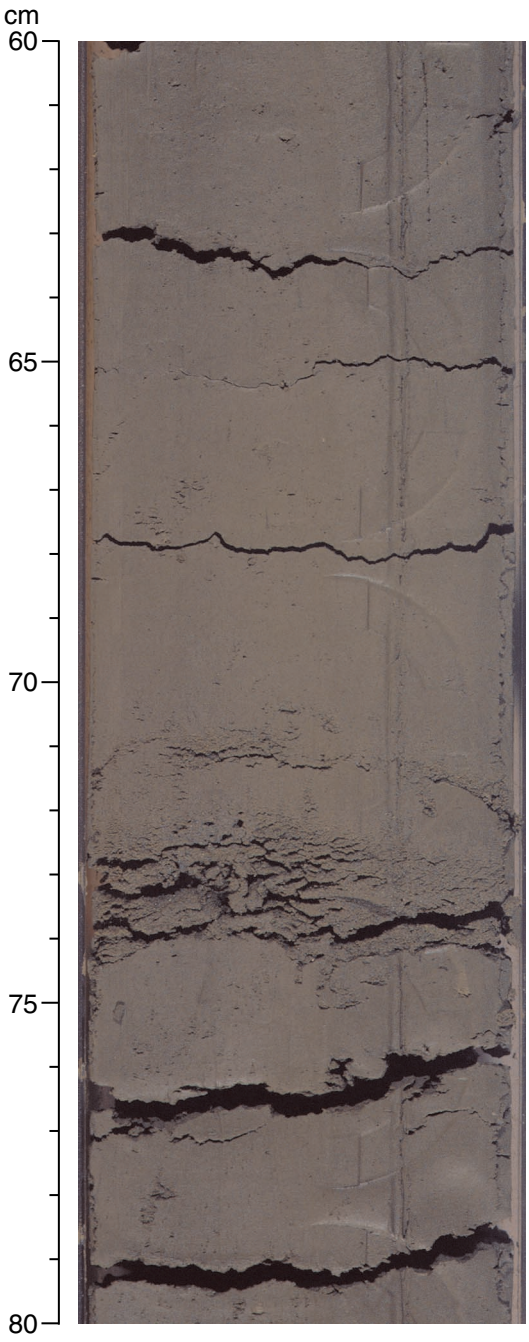

Figure F6. Behavior of magnetic intensity of four samples from Site 1202 over time. Before each measurement samples were magnetized in a 100-mT pulsed field. J_{ini} = magnetic intensity right after core recovery.

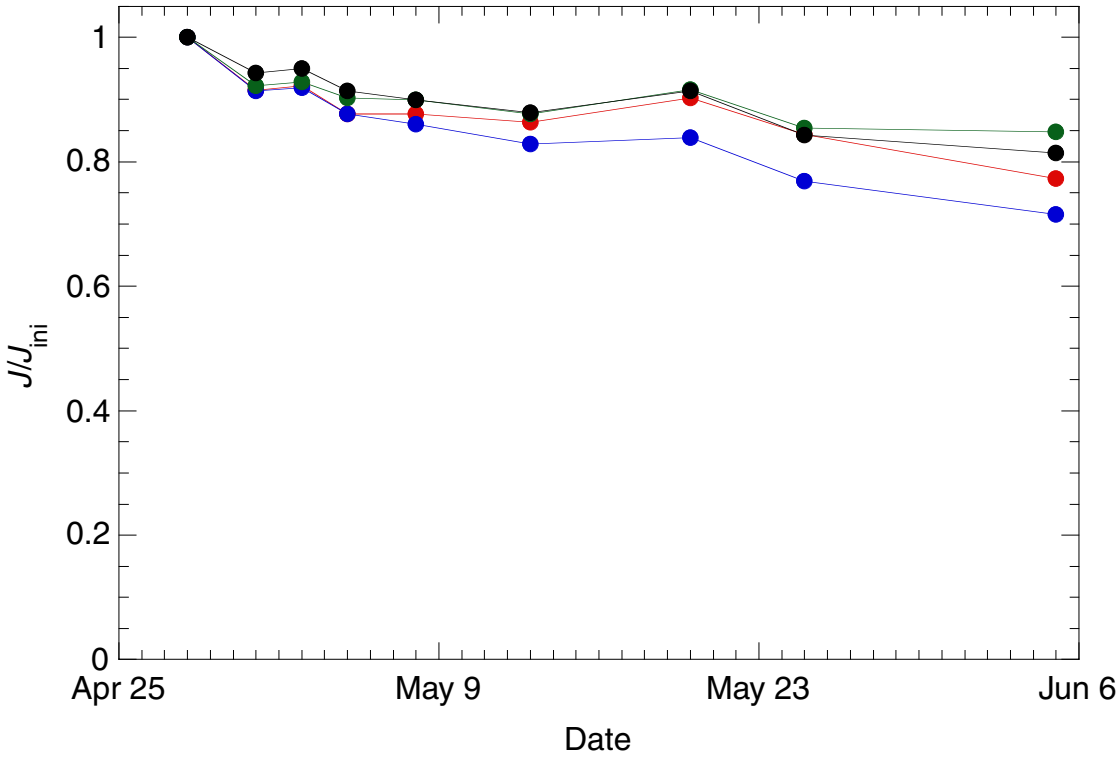

Figure F7. Downcore variations of magnetic inclination and intensity after 20-mT AF demagnetization and magnetic susceptibility. **A.** Hole 1202A. (Continued on next two pages.)

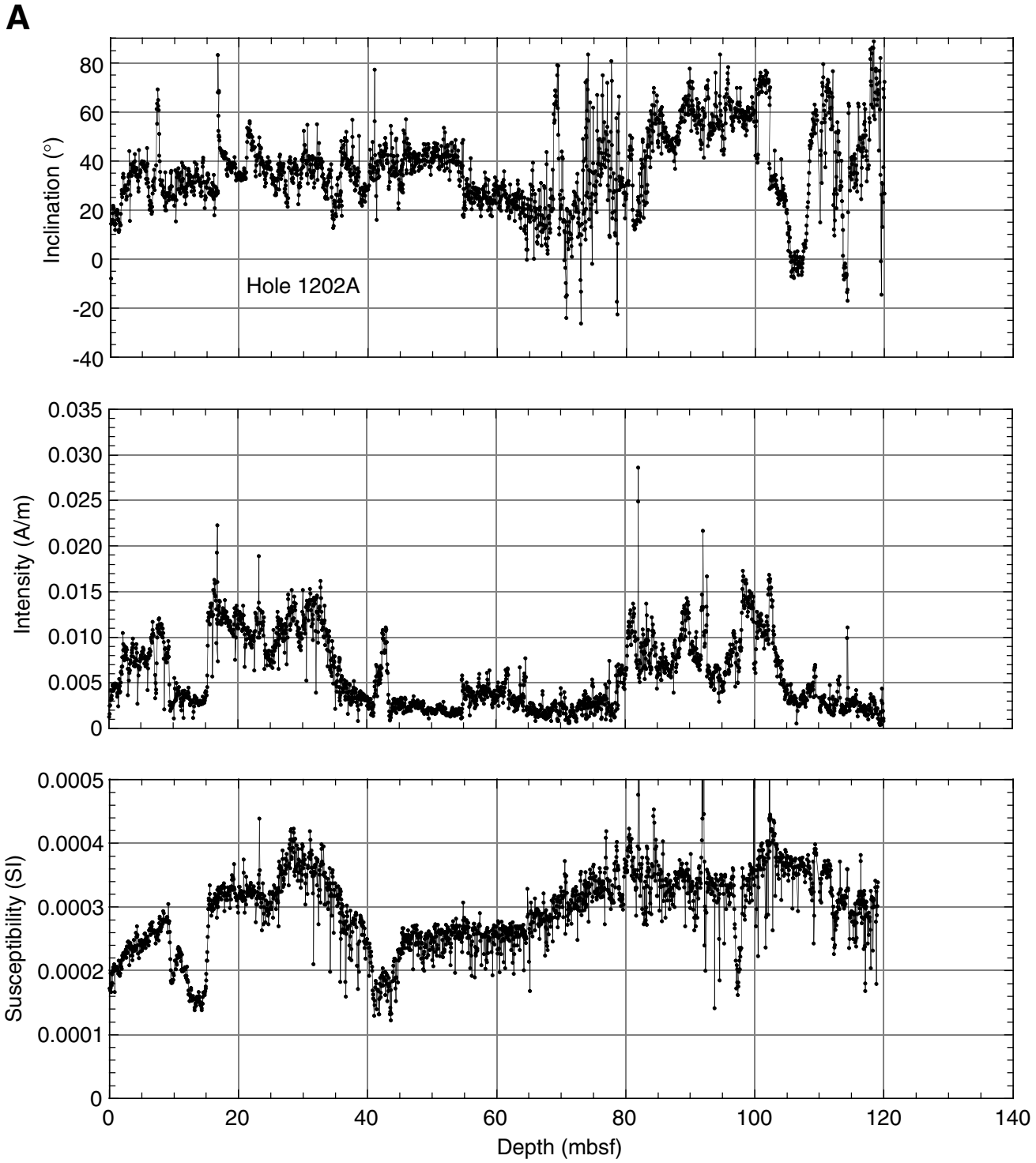

Figure F7 (continued). B. Hole 1202B.

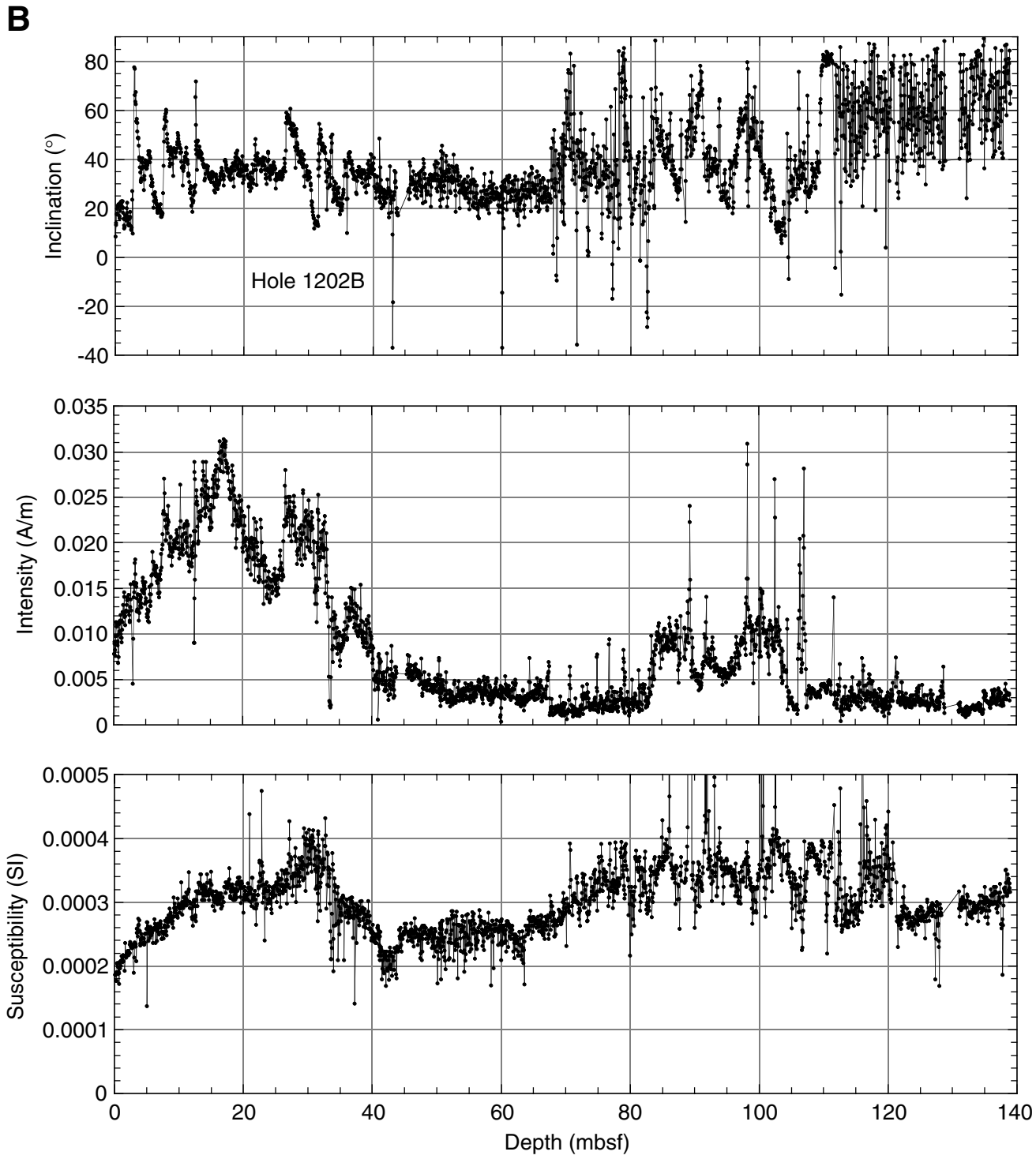

Figure F7 (continued). C. Hole 1202C.

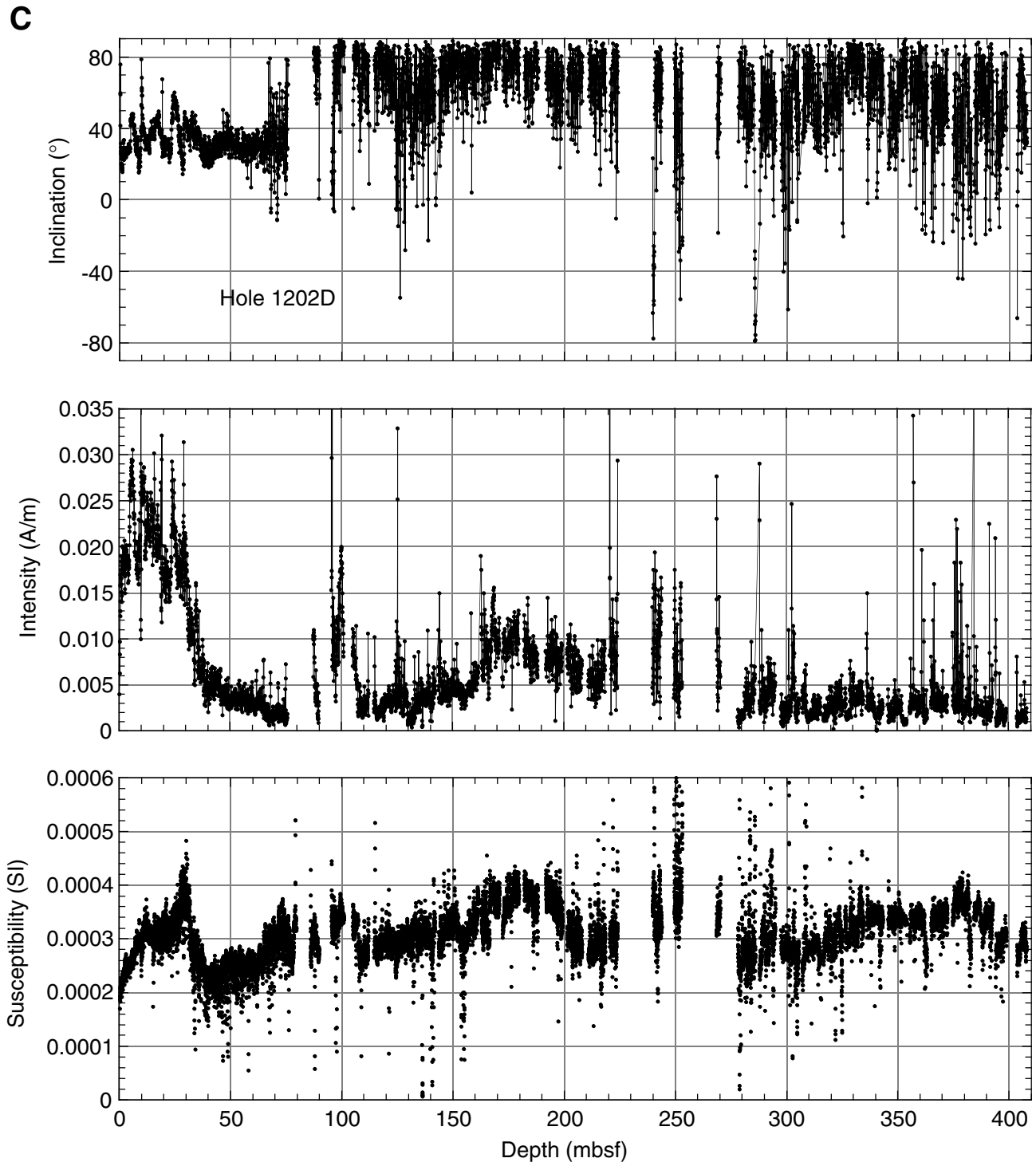

Figure F8. Magnetic susceptibility of Holes 1202A, 1202B, 1202C, and 1202D. An offset of 20, 40, and 60 is applied to the raw instrument units of Holes 1202B, 1202C, and 1202D, respectively.

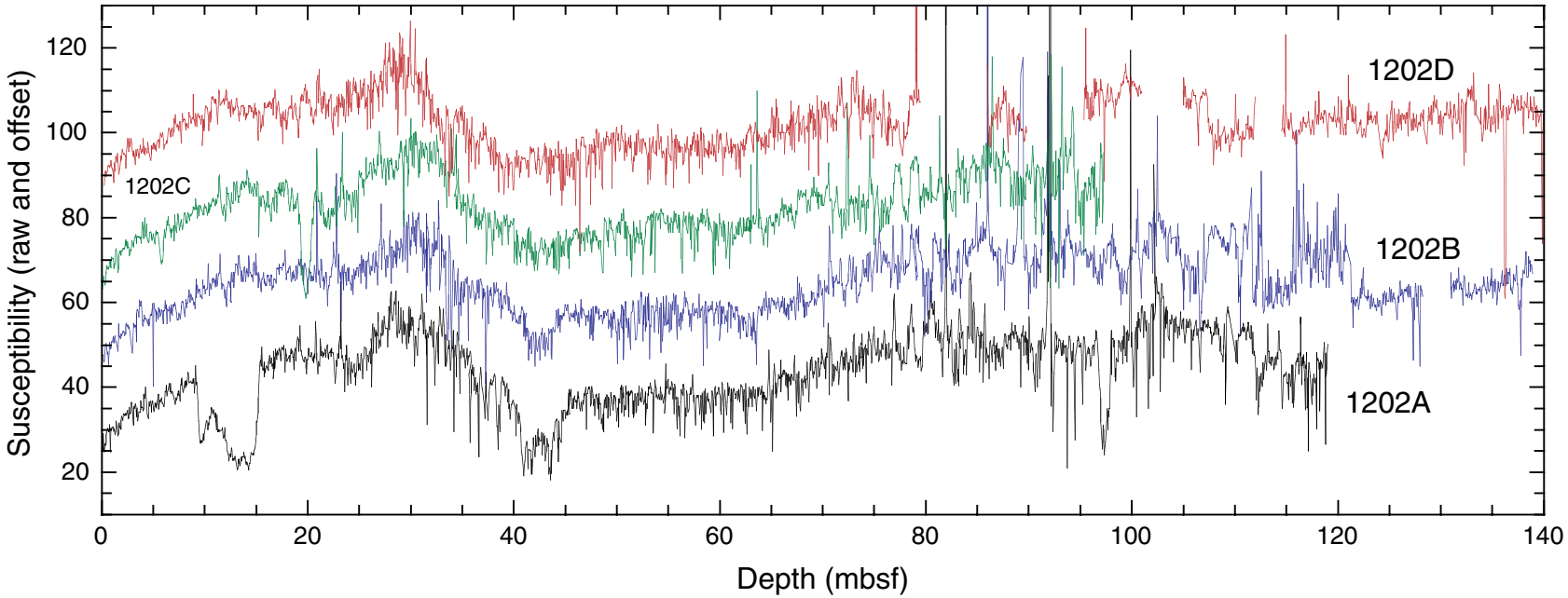

Figure F9. Vector component diagram with normalized intensity decay plots of alternating-field (AF) demagnetization behavior for two samples from Hole 1202A. Open (closed) symbols represent projections onto the vertical (horizontal) plane.

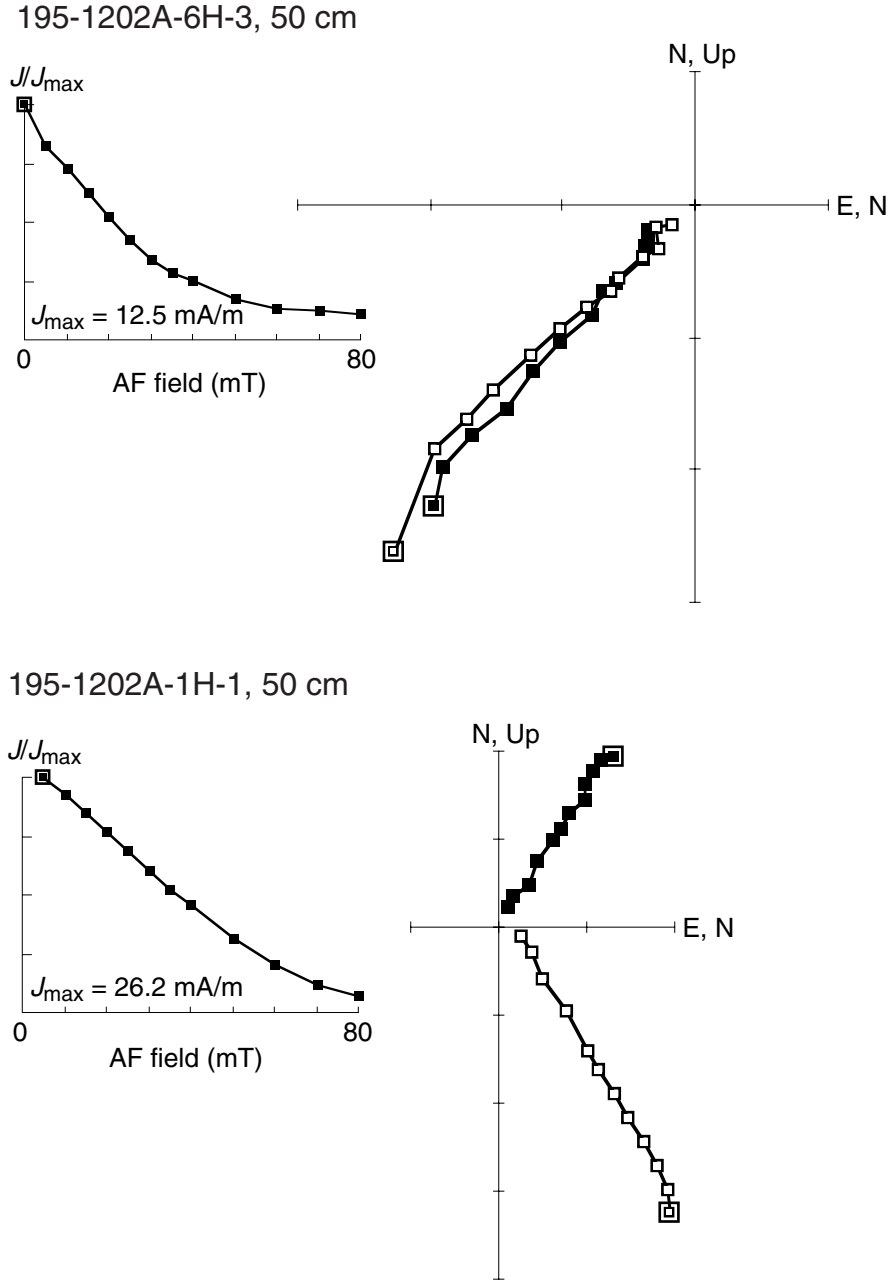

Figure F10. Volume magnetic susceptibility results from the MST in Holes 1202A, 1202B, 1202C, and 1202D, 0–140 mbsf.

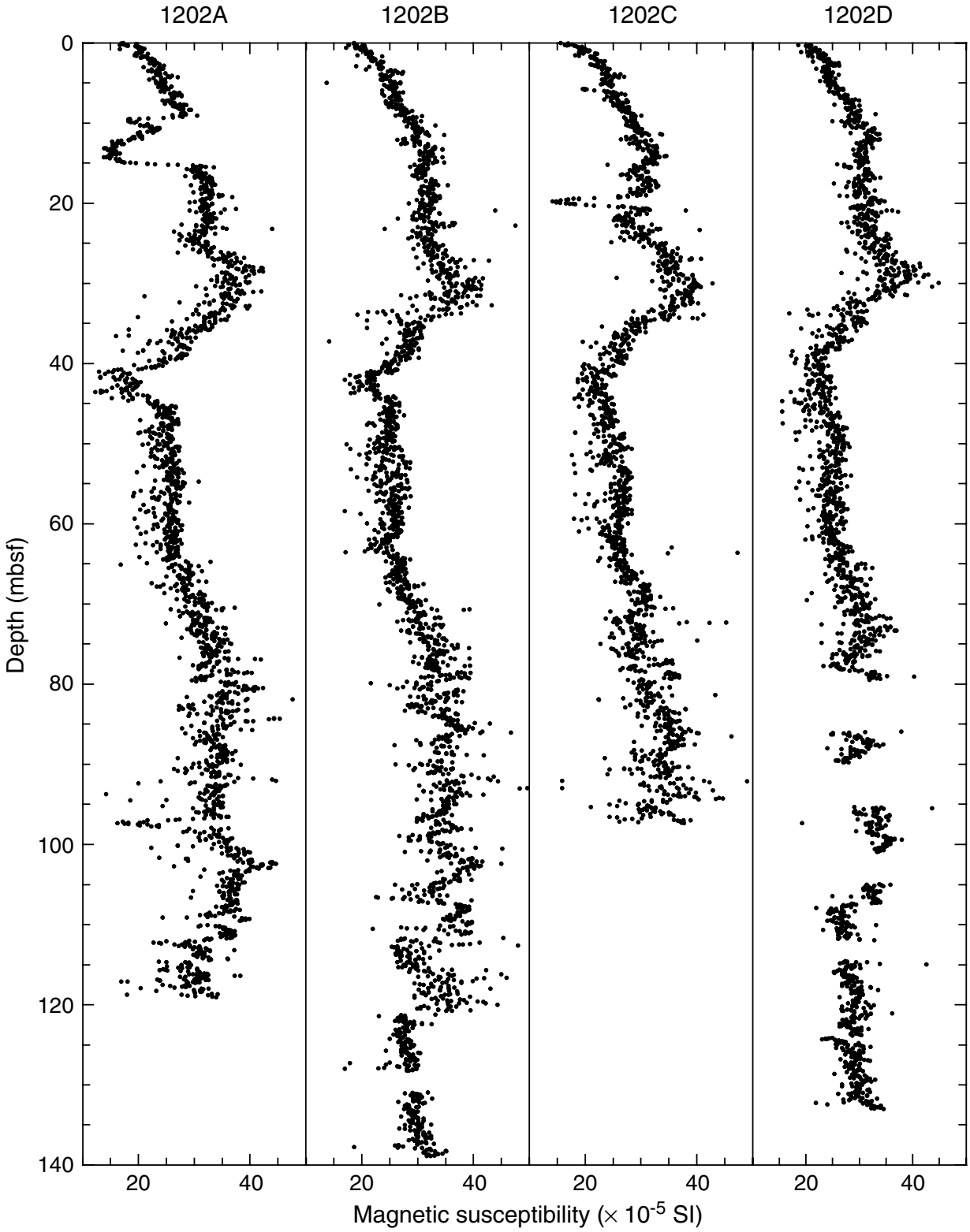

Figure F11. Volume magnetic susceptibility results from the MST for Hole 1202D, 0–420 mbsf.

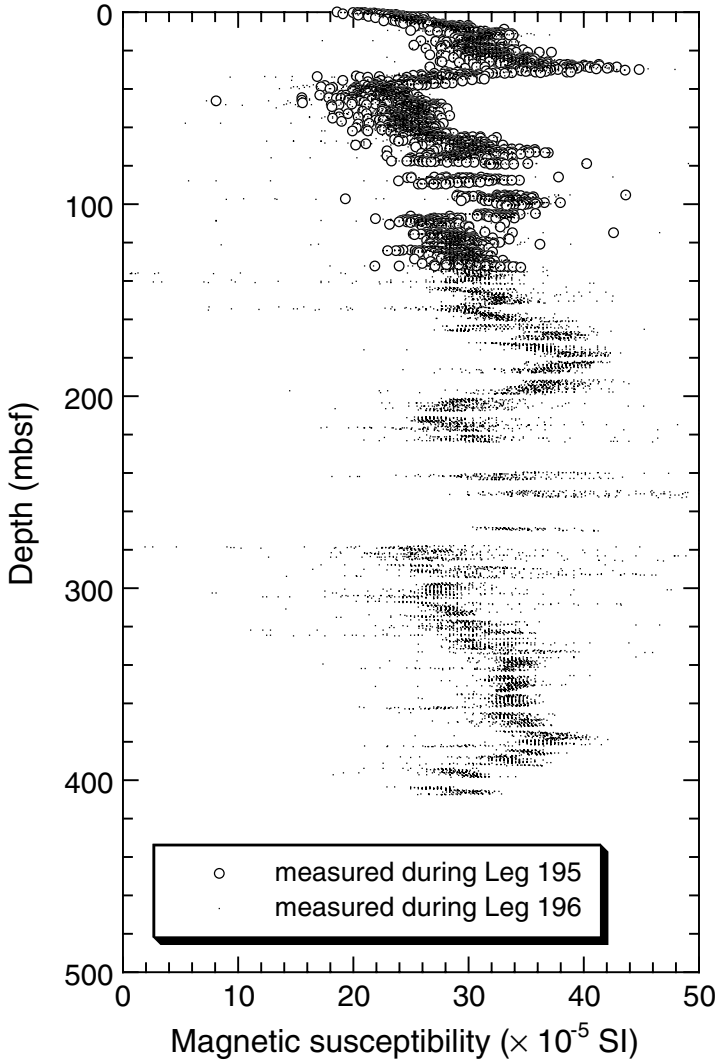

Figure F12. Bulk density results from the MST in Holes 1202A, 1202B, 1202C, and 1202D, 0–140 mbsf.

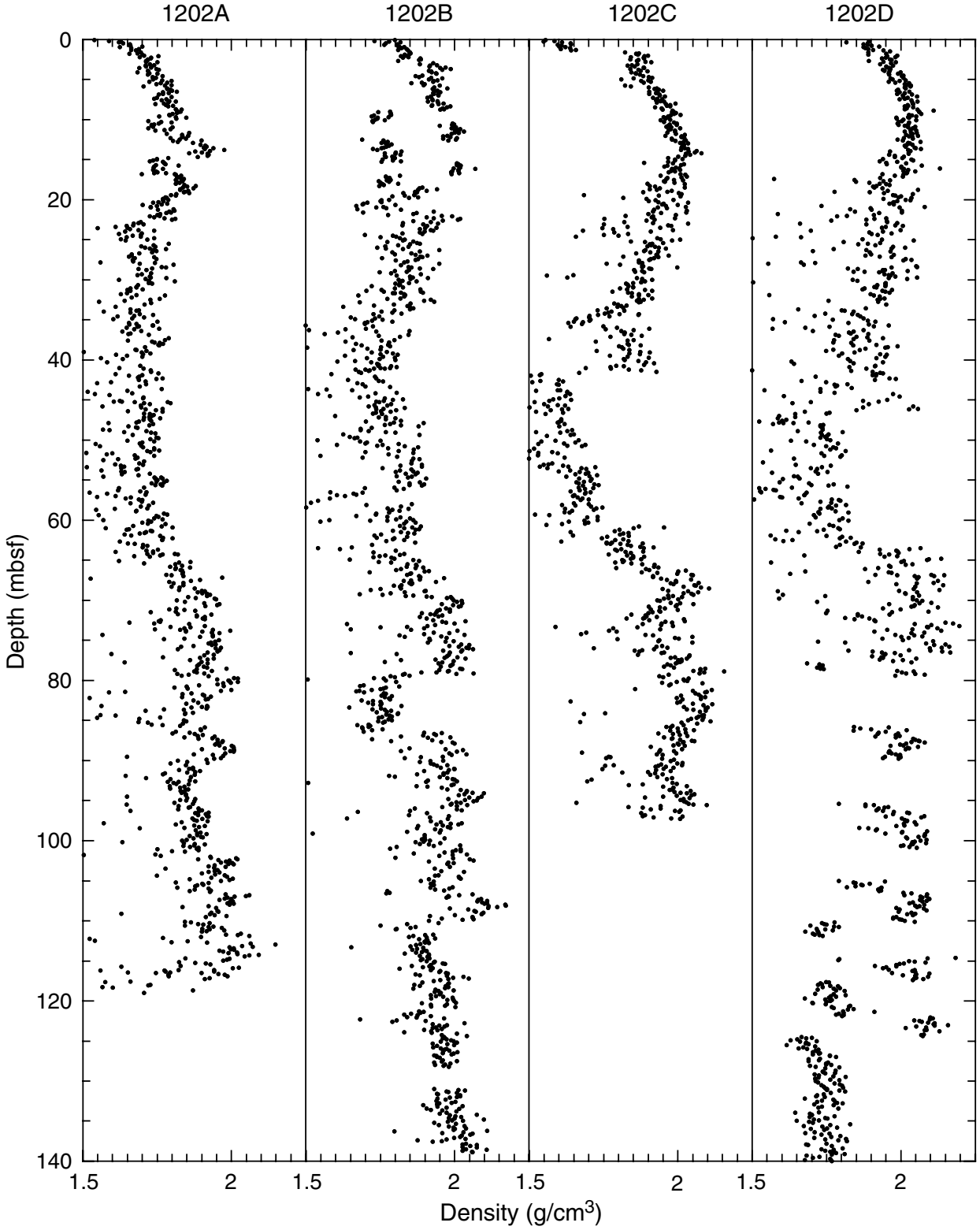

Figure F13. GRA bulk density results for Hole 1202D, 0–420 mbsf.

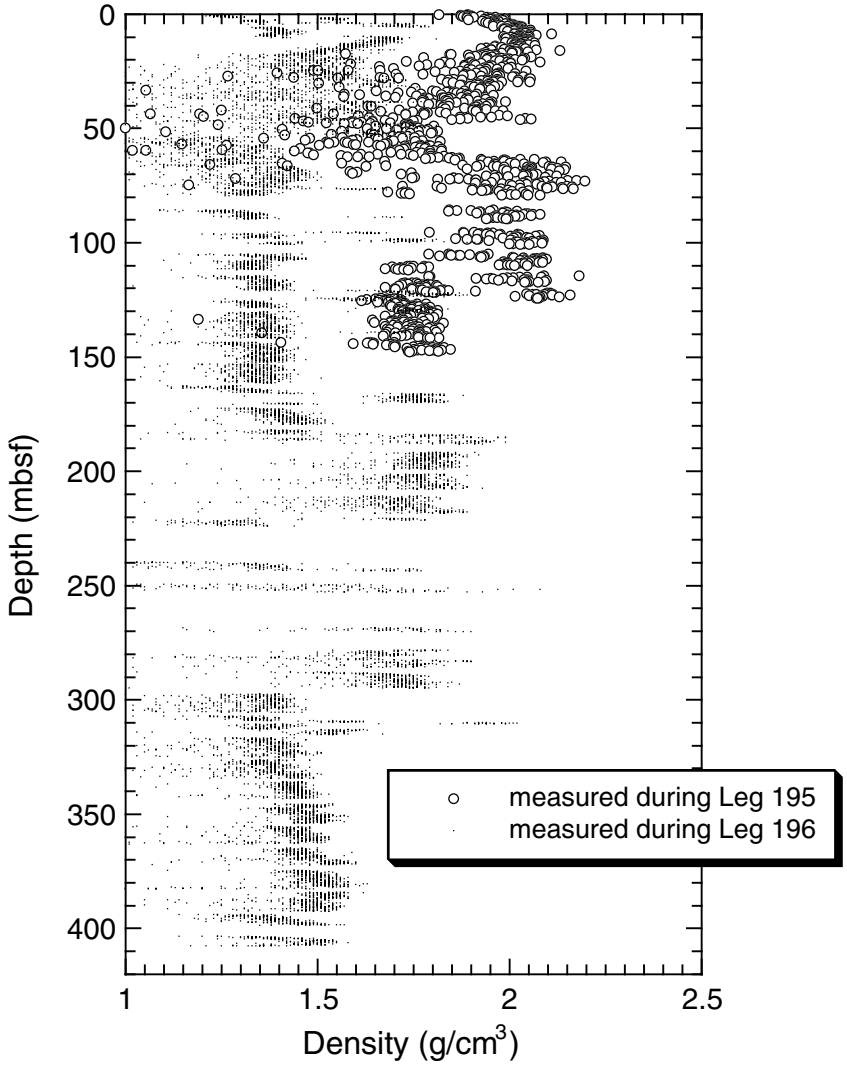

Figure F14. Porosity derived from GRA density measurements at Site 1202, 0–140 mbsf, using Equation 1, p. 12, assuming values of 2.7 g/cm³ for the grain density and 1.0 g/cm³ for the pore water.

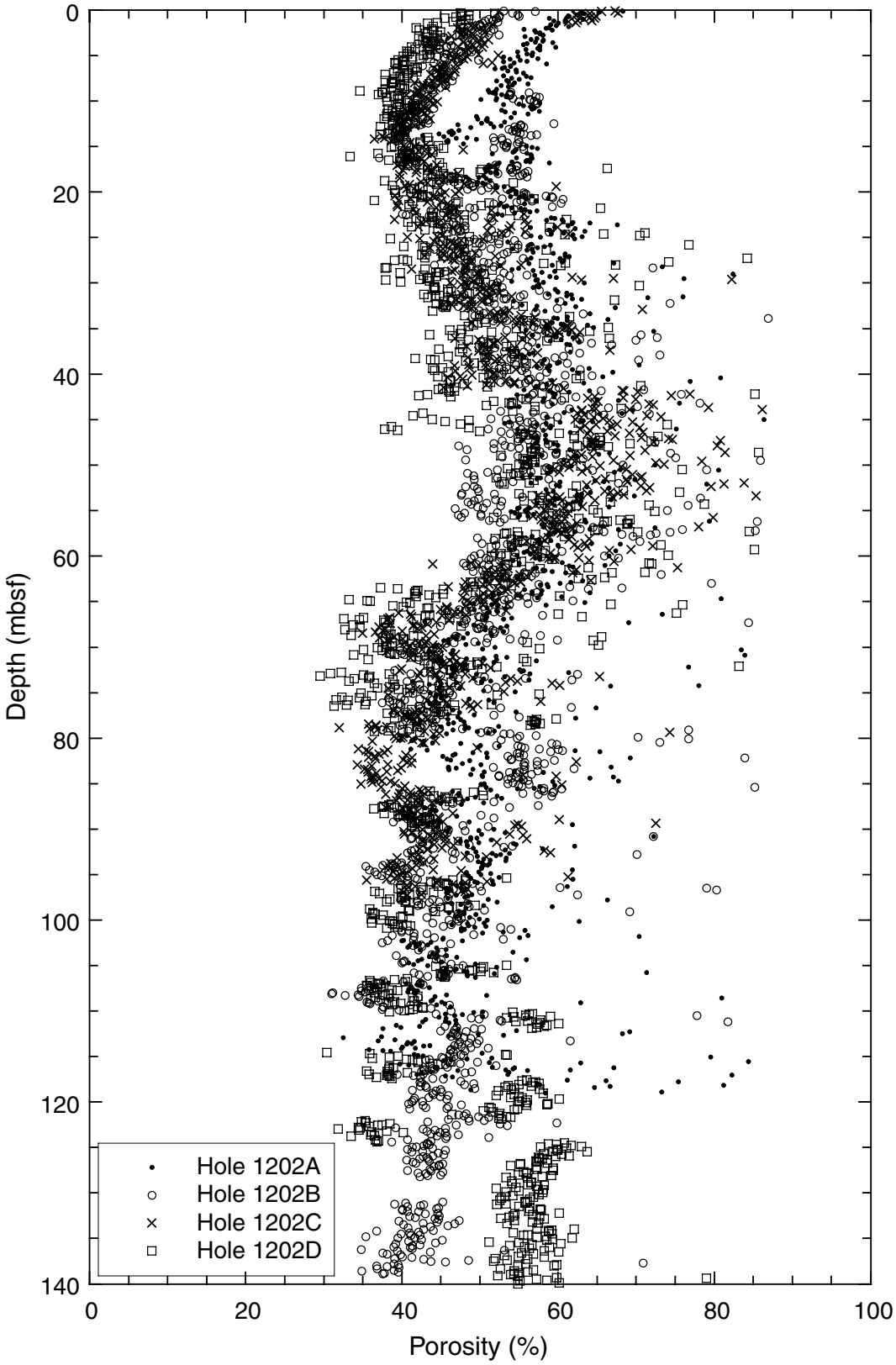

Figure F15. Natural gamma radiation emissions for Hole 1202D, 0–410 mbsf.

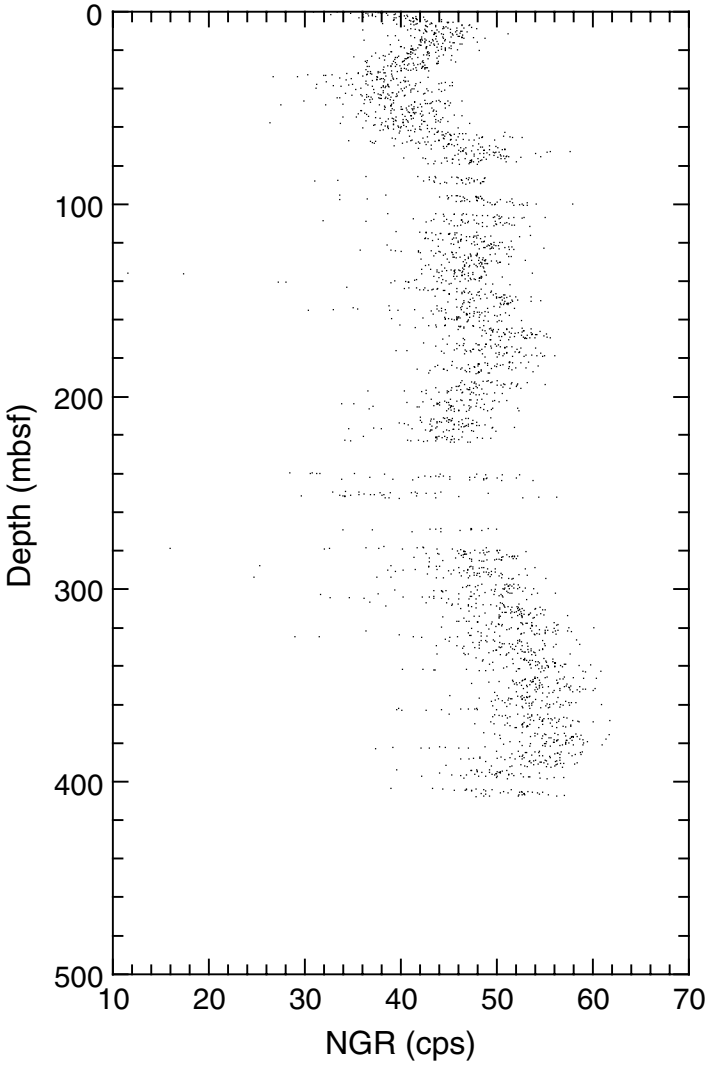

Figure F16. *P*-wave velocity at Site 1202.

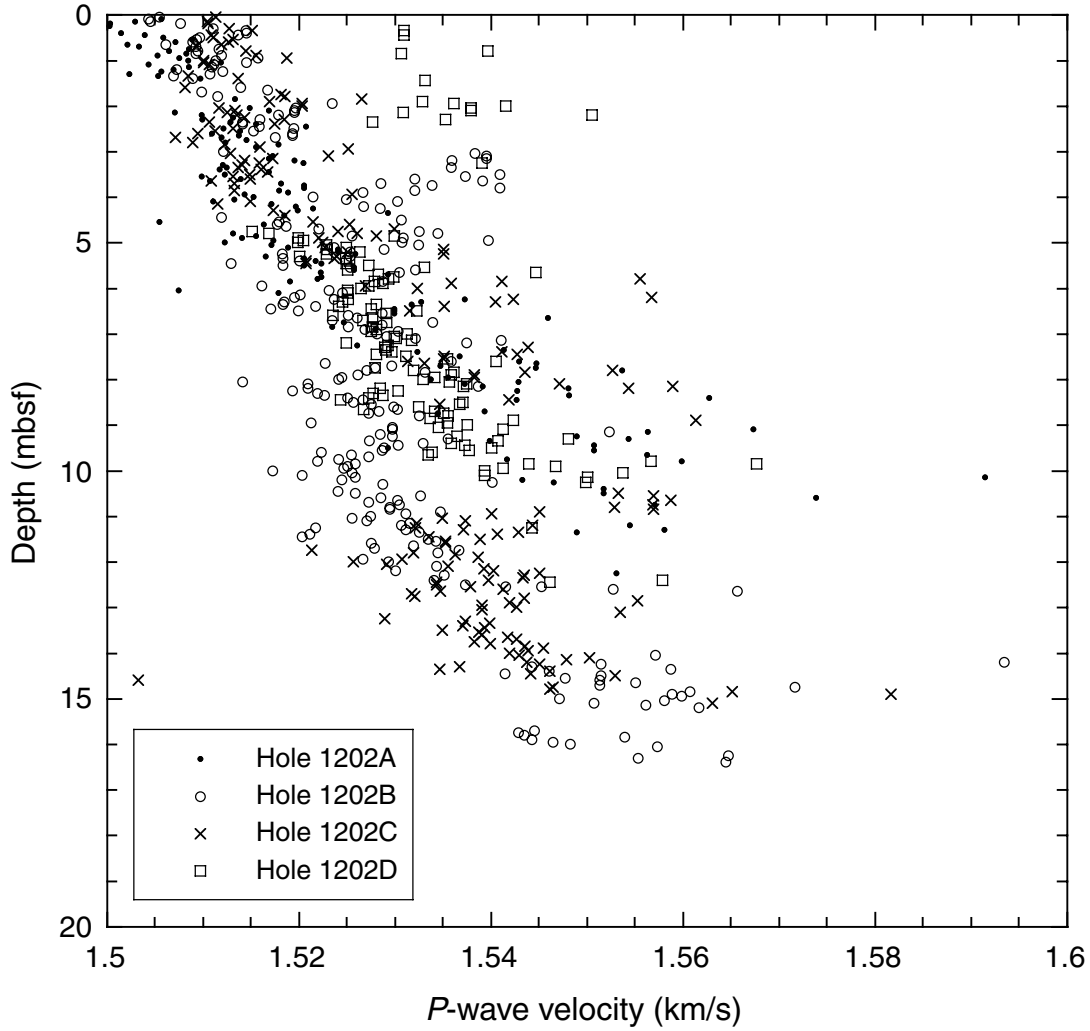

Figure F17. Peak shear strength measured in the sediments from Hole 1202A using the vane shear apparatus.

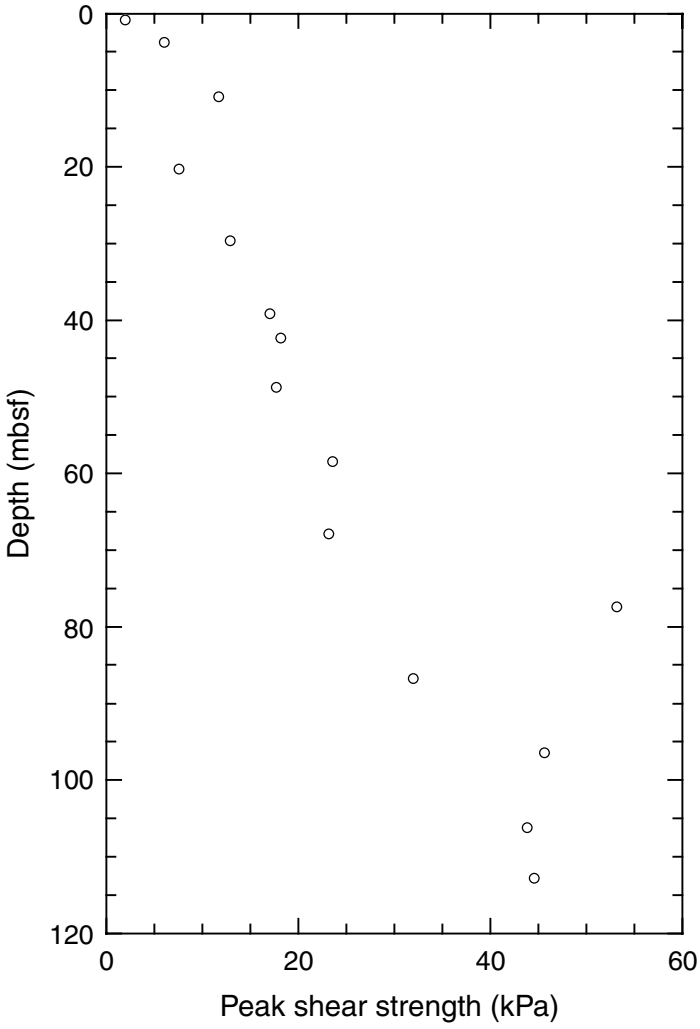

Figure F18. Thermal conductivities measured at Site 1202. The mean value is 1.04 W/(m·K).

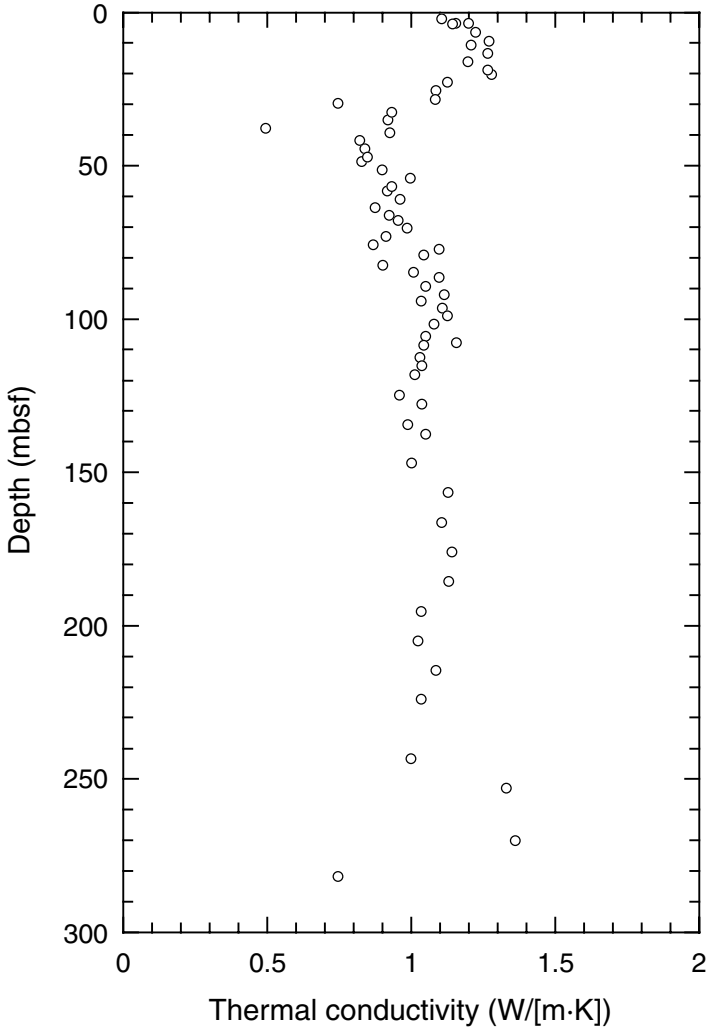

Figure F19. Temperature measurements in Hole 1202A at (**A**) 64.1 mbsf and (**B**) 119.5 mbsf.

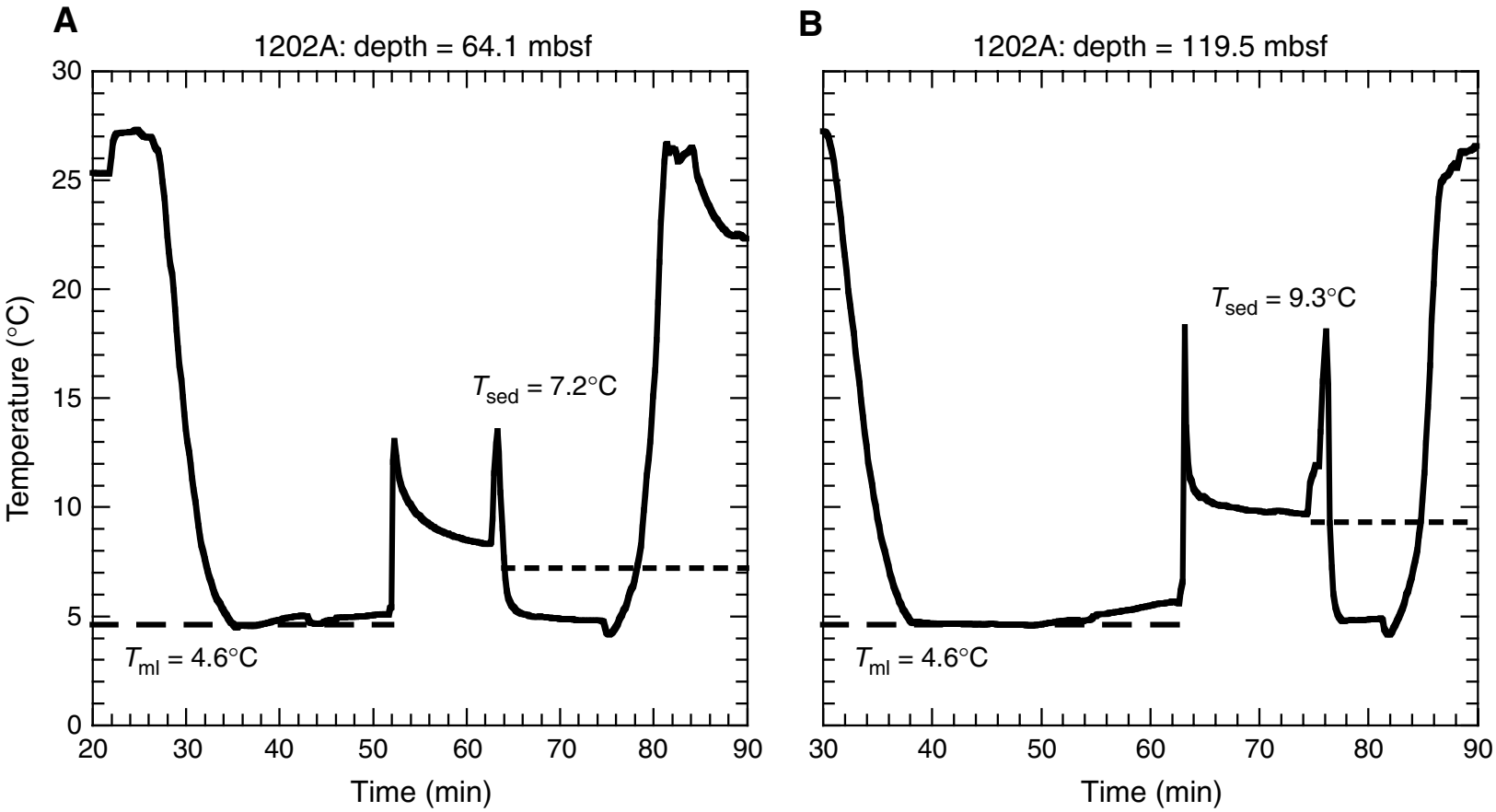

Figure F20. Integrated thermal resistivity vs. depth for Hole 1202A.

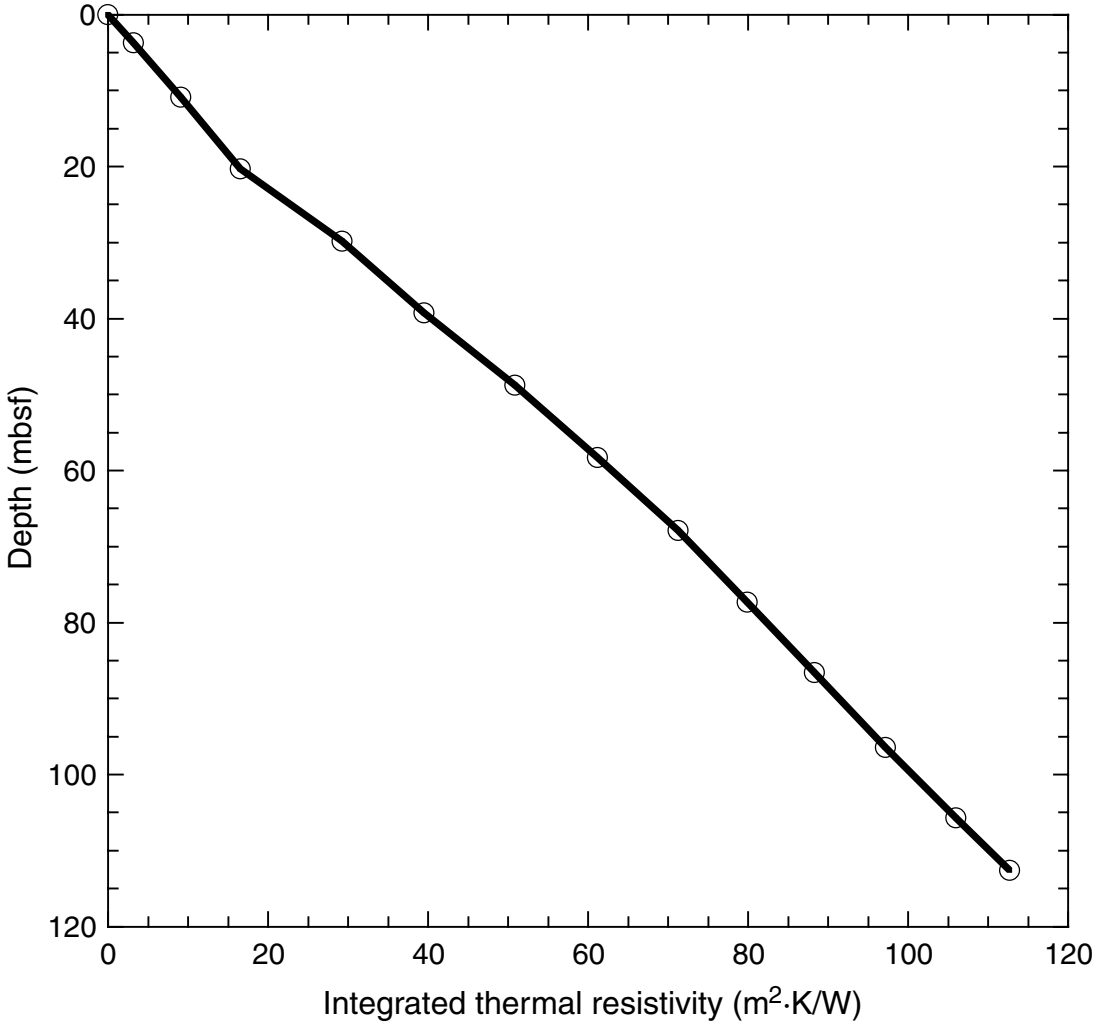

Figure F21. Temperature vs. integrated thermal resistivities, corresponding to equivalent depths, for Hole 1202A.

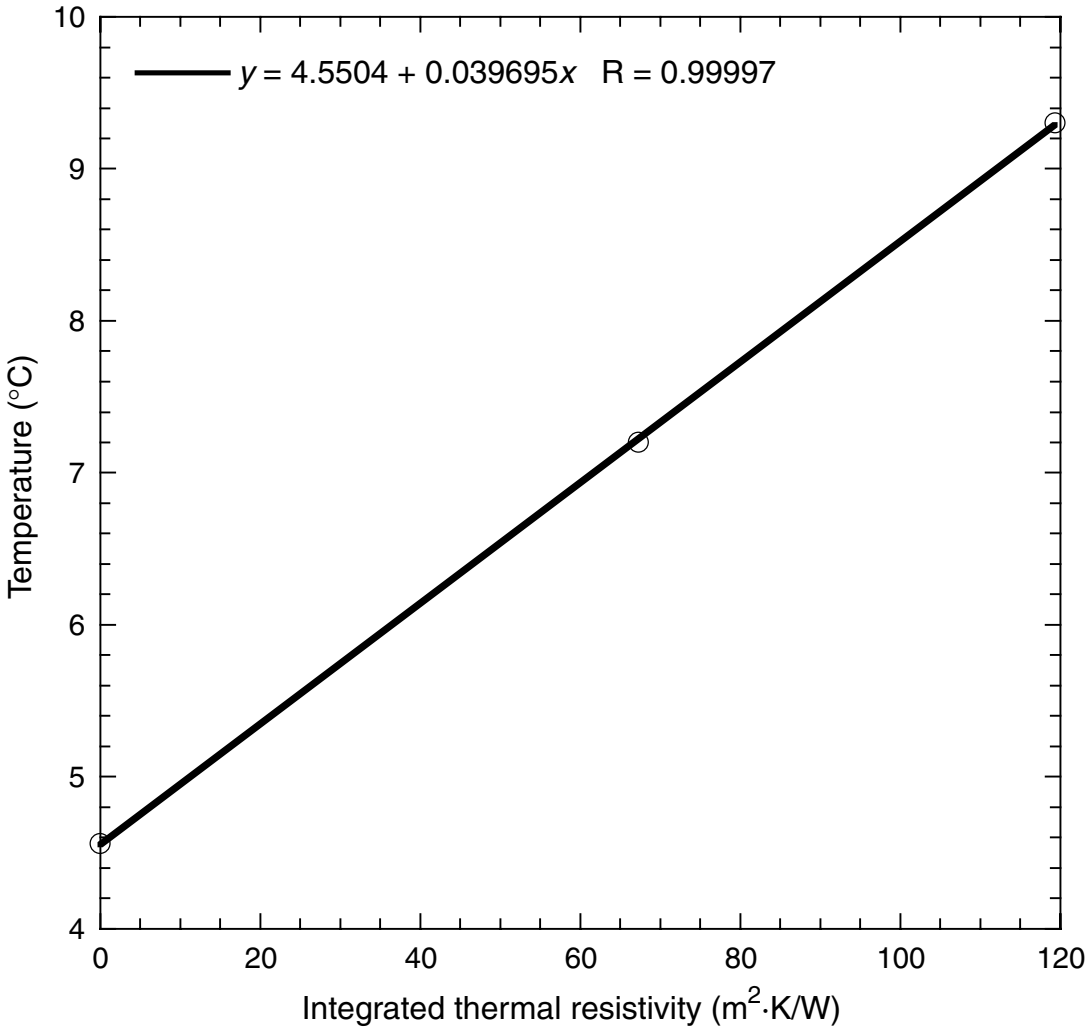

Table T1. Coring summary, Site 1202. (Continued on next two pages.)

Hole 1202A
Latitude: 24°48.2449′N
Longitude 122°30.0002′E
Time on site (hr): 79.25 (0300 hr, 28 Apr–1015 hr, 1 May 2001)
Time on hole (hr): 16.00 (0300 hr, 28 Apr–1900 hr, 28 Apr 2001)
Seafloor (drill pipe measurement from rig floor, mbrf): 1285.8
Distance between rig floor and sea level (m): 11.7
Water depth (drill pipe measurement from sea level, m): 1274.1
Total depth (drill pipe measurement from rig floor, mbrf): 1405.3
Total penetration (meters below seafloor, mbsf): 119.5
Total length of cored section (m): 119.5
Total core recovered (m): 127.14
Core recovery (%): 106.4
Total number of cores: 13

Hole 1202B
Latitude: 24°48.2445′N
Longitude 122°30.0077′E
Time on hole (hr): 9.75 (1900 hr, 28 Apr–0445 hr, 29 Apr 2001)
Seafloor (drill pipe measurement from rig floor, mbrf): 1286.0
Distance between rig floor and sea level (m): 11.9
Water depth (drill pipe measurement from sea level, m): 1274.1
Total depth (drill pipe measurement from rig floor, mbrf): 1426.5
Total penetration (meters below seafloor, mbsf): 140.5
Total length of cored section (m): 140.5
Total core recovered (m): 143.28
Core recovery (%): 102.0
Total number of cores: 16

Hole 1202C
Latitude: 24°48.2428′N
Longitude 122°30.0167′E
Time on hole (hr): 7.5 (0445 hr, 29 Apr–1215 hr, 29 Apr 2001)
Seafloor (drill pipe measurement from rig floor, mbrf): 1285.2
Distance between rig floor and sea level (m): 11.6
Water depth (drill pipe measurement from sea level, m): 1273.6
Total depth (drill pipe measurement from rig floor, mbrf): 1382.7
Total penetration (meters below seafloor, mbsf): 97.5
Total length of cored section (m): 97.5
Total core recovered (m): 102.56
Core recovery (%): 105.2
Total number of cores: 11

Hole 1202D
Latitude: 24°48.2456′N
Longitude 122°30.0259′E
Time on hole (hr): 46.00 (1215 hr, 29 Apr–1015 hr, 1 May 2001)
Seafloor (drill pipe measurement from rig floor, mbrf): 1286.7
Distance between rig floor and sea level (m): 11.60
Water depth (drill pipe measurement from sea level, m): 1275.1
Total depth (drill pipe measurement from rig floor, mbrf): 1696.7
Total penetration (meters below seafloor, mbsf): 410.0
Total length of cored section (m): 410.0
Total core recovered (m): 321.62
Core recovery (%): 78.4
Total number of cores: 44

Core	Date (April 2001)	Time (local)	Depth (mbsf) Top	Depth (mbsf) Bottom	Length (m) Cored	Length (m) Recovered	Recovery (%)	Comment
195-1202A-								
1H	28	0820	0.0	7.1	7.1	7.13	100.4	
2H	28	0900	7.1	16.6	9.5	9.99	105.2	
3H	28	0920	16.6	26.1	9.5	9.96	104.8	
4H	28	1030	26.1	35.6	9.5	10.30	108.4	Oriented
5H	28	1100	35.6	45.1	9.5	10.31	108.5	Oriented
6H	28	1140	45.1	54.6	9.5	10.25	107.9	Oriented
7H	28	1245	54.6	64.1	9.5	10.29	108.3	Oriented
8H	28	1315	64.1	73.6	9.5	10.24	107.8	Oriented
9H	28	1345	73.6	83.1	9.5	10.18	107.2	Oriented
10H	28	1455	83.1	92.6	9.5	10.30	108.4	Oriented
11H	28	1535	92.6	102.1	9.5	10.22	107.6	Oriented

Table T1 (continued).

Core	Date (April 2001)	Time (local)	Depth (mbsf) Top	Depth (mbsf) Bottom	Length (m) Cored	Length (m) Recovered	Recovery (%)	Comment
12H	28	1615	102.1	110.0	7.9	7.90	100.0	Oriented
13H	28	1730	110.0	119.5	9.5	10.07	106.0	Oriented
				Totals:	119.5	127.14	106.4	
195-1202B-								
1H	28	1945	0.0	2.9	2.9	2.88	99.3	
2H	28	2010	2.9	12.4	9.5	9.93	104.5	
3H	28	2035	12.4	21.9	9.5	9.84	103.6	
4H	28	2100	21.9	31.4	9.5	10.22	107.6	Expanding core
5H	28	2125	31.4	40.9	9.5	10.32	108.6	Expanding core
6H	28	2150	40.9	50.4	9.5	10.38	109.3	Expanding core
7H	28	2215	50.4	59.9	9.5	10.23	107.7	Expanding core
8H	28	2240	59.9	69.4	9.5	10.17	107.1	Expanding core
9H	28	2305	69.4	78.9	9.5	10.21	107.5	Expanding core
10H	28	2330	78.9	88.4	9.5	9.44	99.4	Expanding core
11H	28	2355	88.4	97.9	9.5	10.07	106.0	Expanding core
12H	29	0030	97.9	104.2	6.3	6.28	99.7	Expanding core
13H	29	0100	104.2	111.6	7.4	7.44	100.5	Expanding core
14X	29	0225	111.6	121.2	9.6	9.59	99.9	Expanding core
15X	29	0310	121.2	130.9	9.7	7.85	80.9	Expanding core
16X	29	0350	130.9	140.5	9.6	8.43	87.8	Expanding core
				Totals:	140.5	143.28	102.0	
195-1202C-								
1H	29	0555	0.0	5.7	5.7	5.69	99.8	
2H	29	0625	5.7	15.2	9.5	9.73	102.4	
3H	29	0650	15.2	24.7	9.5	9.71	102.2	
4H	29	0720	24.7	34.2	9.5	10.37	109.2	
5H	29	0745	34.2	43.7	9.5	10.44	109.9	
6H	29	0820	43.7	53.2	9.5	10.25	107.9	
7H	29	0855	53.2	62.7	9.5	10.10	106.3	
8H	29	0925	62.7	72.2	9.5	9.92	104.4	
9H	29	0955	72.2	81.0	8.8	8.80	100.0	
10H	29	1040	81.0	90.5	9.5	10.27	108.1	
11H	29	1130	90.5	97.5	7.0	7.28	104.0	
				Totals:	97.5	102.56	105.2	
195-1202D-								
1H	29	1300	0.0	0.2	0.2	0.15	75.0	
2H	29	1320	0.2	9.7	9.5	9.86	103.8	
3H	29	1345	9.7	19.2	9.5	9.84	103.6	
4H	29	1410	19.2	28.7	9.5	10.18	107.2	
5H	29	1435	28.7	38.2	9.5	10.11	106.4	
6H	29	1500	38.2	47.7	9.5	10.45	110.0	
7H	29	1525	47.7	57.2	9.5	10.44	109.9	
8H	29	1550	57.2	66.7	9.5	10.30	108.4	
9H	29	1620	66.7	76.2	9.5	10.34	108.8	
10X	29	1710	76.2	85.7	9.5	3.54	37.3	
11X	29	1740	85.7	95.3	9.6	4.37	45.5	
12X	29	1810	95.3	104.9	9.6	5.94	61.9	
13X	29	1845	104.9	114.5	9.6	7.35	76.6	
14X	29	1910	114.5	124.1	9.6	9.67	100.7	
15X	29	1935	124.1	133.8	9.7	9.66	99.6	
16X	29	2000	133.8	143.4	9.6	8.36	87.1	
17X	29	2025	143.4	153.0	9.6	9.34	97.3	
18X	29	2100	153.0	162.7	9.7	8.75	90.2	
19X	29	2130	162.7	172.3	9.6	8.47	88.2	
20X	29	2200	172.3	182.0	9.7	7.85	80.9	
21X	29	2230	182.0	191.7	9.7	6.76	69.7	
22X	29	2300	191.7	201.3	9.6	8.03	83.7	
23X	29	2340	201.3	210.9	9.6	7.20	75.0	
24X	30	0015	210.9	220.5	9.6	8.23	85.7	
25X	30	0100	220.5	230.1	9.6	3.81	39.7	
26X	30	0135	230.1	239.7	9.6	0.21	2.2	
27X	30	0215	239.7	249.3	9.6	4.30	44.8	
28X	30	0320	249.3	258.9	9.6	3.99	41.6	
29X	30	0410	258.9	268.5	9.6	0.00	0.0	
30X	30	0455	268.5	278.1	9.6	2.04	21.3	
31X	30	0600	278.1	287.8	9.7	8.37	86.3	
32X	30	0700	287.8	297.4	9.6	7.35	76.6	

Table T1 (continued).

Core	Date (April 2001)	Time (local)	Depth (mbsf) Top	Depth (mbsf) Bottom	Length (m) Cored	Length (m) Recovered	Recovery (%)	Comment
33X	30	0840	297.4	307.0	9.6	8.53	88.9	
34X	30	1055	307.0	316.6	9.6	8.57	89.3	
35X	30	1200	316.6	326.2	9.6	8.69	90.5	
36X	30	1240	326.2	335.9	9.7	9.18	94.6	
37X	30	1330	335.9	345.6	9.7	8.37	86.3	
38X	30	1430	345.6	355.3	9.7	9.12	94.0	
39X	30	1525	355.3	364.9	9.6	7.97	83.0	
40X	30	1600	364.9	374.6	9.7	8.52	87.8	
41X	30	1645	374.6	384.2	9.6	8.77	91.4	
42X	30	1735	384.2	393.9	9.7	8.75	90.2	
43X	30	1815	393.9	403.5	9.6	5.29	55.1	
44X	30	1925	403.5	410.0	6.5	4.60	70.8	
				Totals:	410.0	321.62	78.4	

Table T2. Distribution of calcareous nannofossils, Site 1202. (**See table notes.** Continued on next page.)

Core, section, interval (cm)	Depth (mbsf)	Zone	Preservation	Group abundance	*Braarudosphaera bigelowii*	*Calcidiscus leptoporus*	*Ceratolithus cristatus*	*Coccolithus pelagicus*	*Discoaster brouweri*	*Discoaster pentaradiatus*	*Discosphaera tubifera*	*Emiliania huxleyi*	*Florisphaera profunda*	*Gephyrocapsa caribbeanica*	*Gephyrocapsa margerelii*	*Gephyrocapsa oceanica*	*Gephyrocapsa* spp. (small)	*Helicosphaera carteri*	*Neosphaera coccolithomorpha*	*Pontosphaera multiforata*	*Pontosphaera* spp.	*Pseudoemiliania lacunosa*	*Reticulofenestra* sp.	*Rhabdosphaera clavigera*	*Scapholithus fossilis*	*Syracosphaera pulchra*	*Syracosphaera* spp.	*Umbellosphaera* spp.	*Umbilicosphaera sibogae*
195-1202A-																													
1H-CC, 9–14	7.08	NN21	G	C								A	A			A			F								C		C
2H-CC, 14–19	17.04	NN21	G	C		R						D	A			C		R	R					R			F		F
3H-CC, 14–19	26.51	NN21	G	C		R						A	A			C		F								R	F	F	F
4H-CC, 38–43	36.35	NN21	G	C								A	A			A		F						R		R	F		C
5H-CC, 37–42	45.86	NN21	M	C		R						A	C			C	R						F			R			R
6H-CC, 45–50	55.30	NN21	G	F								C	C			F								R		R	R		
7H-CC, 49–54	64.84	NN21	M	C								C	C			C								R		R	R		R
8H-CC, 29–34	74.29	NN21	M	F								F	C			F				R									
9H-CC, 33–38	83.73	NN21	G	C					R	R		C	C	R		C	R	R				R		F		R	R		R
10H-CC, 54–58	93.36	NN21	G	C								C	C		R	F			R			R	R	R		R	R		
11H-CC, 40–44	102.78	NN21	G	C		R						F	C			F								R		R		R	R
12H-CC, 35–40	109.95	NN21	G	F		R		R				F																	R
13H-CC, 90–95	120.02	NN21	G	C	R	R						F			F	F	R										R		
195-1202B-																													
1H-CC, 6–10	2.84	NN21	M	C		R						A	A			C								R					
2H-CC, 10–14	12.79	NN21	G	C		R		R				A	C			C			R						R	F		R	
3H-CC, 21–25	22.20	NN21	M	F		R						A	A			C		R								R			R
4H-CC, 29–33	32.08	NN21	G	C								A	A			C							R			R		R	R
5H-CC, 38–42	41.68	NN21	G	C	R							A			R	R		R									R	R	R
6H-CC, 44–48	51.24	NN21	G	F								F	F	R		F											R		
7H-CC, 28–31	60.60	NN21	G	C								F	F		F	F													
8H-CC, 32–36	70.03	NN21	G	F								F	F			F							R	R					R
9H-CC, 27–31	79.57	NN21	G	F		R						F				F								R					
10H-CC, 32–36	88.30	NN21	G	C								C	R			R		R							R	F	F		
11H-CC, 34–39	98.42	NN21	G	F		R					R	C				C		R					R	R					
12H-CC, 17–22	104.14	NN21	G	C								C				C	R							R	R	R	F		
13H-CC, 27–32	111.59	NN21	G	C								C				F		R						R		R			R
14X-CC, 28–33	121.14	NN21	G	A		R						A				A													R
15X-CC, 15–20	129.00	NN21	G	A			R	R				A				C		R					R				R		R
16X-CC, 31–36	139.28	NN21	G	F								A				C								R					
195-1202D-																													
15X-CC, 15–19	133.72	NN21	G	F								F				C	F							R			F		
17X-CC, 14–18	152.70	NN21	G	R								C				F												R	
18X-CC, 17–21	161.71	NN21	G	F								F				F	F							R			R		
19X-CC, 16–20	171.13	NN21	G	F		R						C				F								R			R		R
20X-CC, 43–47	180.11	NN21	G	F		R						A				C		R									C		R
21X-CC, 47–51	188.72	NN21	G	C								C				F		R				R	R	R		R	R		R
22X-CC, 36–40	199.69	NN21	G	R								R				R													
23X-CC, 38–42	208.46	NN21	G	F		R	R					F		F		F	F	R						R					
24X-CC, 54–59	219.08	NN21	G	R								R		R		R	R												
25X-CC, 13–18	224.26	NN21	G	T								R			R	R	R												
26X-CC, 16–21	230.26	NN21	G	T								R			R	R	R												
27X-CC, 8–13	243.95	NN21	M	R								R		R		R		R											R
28X-CC, 9–14	253.24	NN21		B																									
30X-CC, 14–19	270.49	NN21	M	T								R				R													
31X-CC, 42–47	286.42	NN21	G	R								R				F	R										R		
32X-CC, 9–14	295.10	NN21	G	R		R						C				A	F	F						R			R		
33X-CC, 21–26	305.88	NN21	G	F		R	R					C				A	F	F									F		R
34X-CC, 10–15	315.52	NN21	G	C			R					C				A		C						R					R
35X-6, 131–136	325.24	NN21	G	F								F				F		F											
36X-CC, 76–81	335.33	NN21	G	F								F		F		F		R						R			R		R
37X-CC, 88–92	344.23	NN21	G	R								F				F													
38X-CC, 54–57	354.69	NN21	G	R								F			R	F		R						R			R		
39X-6, 115–119	363.23	NN21	G	R								R				R	R	R						R			R		
40X-CC, 102–106	373.38	NN21	G	R			R					F				F													
41X-CC, 33–38	383.32	NN21	G	R		R						F				R		R											
42X-CC, 21–25	392.91	NN21	G	R		R		R				F		R		F	R	R			R						R		

Table T2 (continued).

Core, section, interval (cm)	Depth (mbsf)	Zone	Preservation	Group abundance	*Braarudosphaera bigelowii*	*Calcidiscus leptoporus*	*Ceratolithus cristatus*	*Coccolithus pelagicus*	*Discoaster brouweri*	*Discoaster pentaradiatus*	*Discosphaera tubifera*	*Emiliania huxleyi*	*Florisphaera profunda*	*Gephyrocapsa caribbeanica*	*Gephyrocapsa margarelii*	*Gephyrocapsa oceanica*	*Gephyrocapsa* spp. (small)	*Helicosphaera carteri*	*Neosphaera coccolithomorpha*	*Pontosphaera multiforata*	*Pontosphaera* spp.	*Pseudoemiliania lacunosa*	*Reticulofenestra* sp.	*Rhabdosphaera clavigera*	*Scapholithus fossilis*	*Syracosphaera pulchra*	*Syracosphaera* spp.	*Umbellosphaera* spp.	*Umbilicosphaera sibogae*
43X-CC, 30–34	399.15	NN21	G	T				R				F		R		F													
44X-CC, 9–13	408.06	NN21	G	T								R		R		R						R					R		

Notes: Preservation: G = good, M = moderate. Abundance: A = abundant, C = common, F = few, T = trace, B = barren, D = dominant.

Table T3. Physical properties, Holes 1202A, 1202B, 1202C, and 1202D.

Core, section, interval (cm)	Depth (mbsf)	Thermal conductivity (W/[m·K])	Peak shear strength (kPa)
195-1202A-			
1H-1, 86–86	0.86		2.00
1H-3, 75–75	3.75	1.16	
1H-3, 80–80	3.80		6.10
2H-3, 75–75	10.85	1.21	
2H-3, 80–80	10.90		11.75
3H-3, 75–75	20.35	1.28	7.65
4H-3, 57–57	29.67		12.97
4H-3, 75–75	29.85	0.75	
5H-3, 65–65	39.25		17.08
5H-3, 73–73	39.33	0.93	
5H-5, 78–78	42.38		18.19
6H-3, 70–70	48.80	0.83	17.74
7H-3, 70–70	58.30	0.92	
7H-3, 85–85	58.44		23.62
8H-3, 80–80	67.90	0.96	
8H-3, 86–86	67.96		23.18
9H-3, 75–75	77.35	1.10	
9H-3, 83–83	77.43		53.23
10H-3, 60–60	86.60	1.10	
10H-3, 80–80	86.80		32.05
11H-3, 85–85	96.45	1.11	
11H-3, 86–86	96.46		45.69
12H-3, 60–60	105.70	1.05	
12H-3, 118–118	106.28		43.91
13H-3, 60–60	112.65	1.03	
13H-3, 77–77	112.82		44.58
195-1202B-			
1H-2, 75–75	2.25	1.11	
2H-3, 75–75	6.65	1.23	
3H-3, 75–75	16.15	1.20	
4H-3, 75–75	25.65	1.09	
5H-3, 77–77	35.17	0.92	
6H-3, 80–80	44.70	0.84	
7H-3, 75–75	54.15	1.00	
8H-3, 83–83	63.73	0.88	
9H-3, 75–75	73.15	0.92	
10H-3, 75–75	82.54	0.90	
11H-3, 74–74	92.14	1.12	
12H-3, 75–75	101.65	1.08	
13H-3, 75–75	107.95	1.16	
14X-3, 75–75	115.35	1.04	
15X-3, 75–75	124.95	0.96	
16X-3, 75–75	134.65	0.99	

Core, section, interval (cm)	Depth (mbsf)	Thermal conductivity (W/[m·K])	Peak shear strength (kPa)
195-1202C-			
1H-3, 75–75	3.75	1.20	
2H-3, 75–75	9.45	1.27	
3H-3, 75–75	18.95	1.27	
4H-3, 80–80	28.50	1.09	
5H-3, 78–78	37.98	0.50	
6H-3, 75–75	47.45	0.85	
7H-3, 75–75	56.95	0.93	
8H-3, 75–75	66.45	0.92	
9H-3, 80–80	76.00	0.87	
10H-3, 75–75	84.75	1.01	
11H-3, 75–75	94.25	1.04	
195-1202D-			
2H-3, 75–75	3.95	1.15	
3H-3, 75–75	13.45	1.27	
4H-3, 65–65	22.85	1.13	
5H-3, 90–90	32.60	0.93	
6H-3, 75–75	41.95	0.82	
7H-3, 77–77	51.47	0.90	
8H-3, 85–85	61.05	0.96	
9H-3, 80–80	70.50	0.99	
10X-3, 50–50	79.20	1.04	
11X-3, 75–75	89.45	1.05	
12X-3, 75–75	99.05	1.13	
13X-3, 75–75	108.65	1.05	
14X-3, 75–75	118.25	1.01	
15X-3, 75–75	127.85	1.04	
16X-3, 75–75	137.55	1.05	
17X-3, 75–75	147.15	1.00	
18X-3, 75–75	156.63	1.13	
19X-3, 75–75	166.45	1.11	
20X-3, 75–75	176.05	1.14	
21X-3, 75–75	185.75	1.13	
22X-3, 75–75	195.45	1.04	
23X-3, 80–80	205.10	1.03	
24X-3, 75–75	214.65	1.09	
25X-3, 55–55	224.05	1.04	
27X-3, 75–75	243.45	1.00	
28X-3, 75–75	253.05	1.33	
30X-2, 30–30	270.30	1.36	
31X-3, 75–75	281.85	0.75	